

High Signal-to-Noise Ratio Event-Driven MEMS Motion Sensing

Mohammad Mousavi, Mohammad Alzgool, Benyamin Davaji, and Shahrzad Towfighian*

Two solutions for improving MEMS triboelectric vibration sensors performance in contact-separation mode are reported experimentally and analytically. Triboelectric sensors have mostly been studied in the mesoscale. The gap variation between the electrodes induces a potential difference that represents the external vibration. Miniaturizing the device limits the sensor output because of the limited gap. This work offers a warped MEMS diaphragm constrained on its edges. The dome-shaped structure provides one order of magnitude larger displacement after contact-separation than standard designs resulting in one order of magnitude greater voltage and signal-to-noise-ratio. Second, micro triboelectric sensors do not operate unless the external vibration is sufficiently forceful to initiate contact between layers. The proposed constraints on the edge of the diaphragm provide friction during periodic motion and generate charges. The combination of the warped diaphragm and boundary constraints instead of serpentine springs increases the charge density and voltage generation. The mechanical properties and electrical output are thoroughly investigated including nonlinearity, sensitivity, and signal-to-noise ratio. A sensitivity of 250 mV g⁻¹ and signal-to-noise-ratio of 32 dB is provided by the presented device at resonance, which is very promising for event-driven motion sensors because it does not require signal conditioning and therefore simplifies the sensing circuitry.

1. Introduction

Continuous vibration monitoring is a viable method for diagnosis of mechanical structures potential failure in machinery. For example, a diagnostic method for potential mechanical failure in car components is based on measuring the vibrations on the gear housing and the gear backlash. [1,2] Safety of mechanical motors can be ensured by integrating vibration and temperature sensors, which reduce the motor speed if threshold values are exceeded. [3]

M. Mousavi, M. Alzgool, S. Towfighian
Mechanical Engineering
Binghamton University
4400 Vestal Parkway East, Binghamton, NY 13902, USA
E-mail: stowfigh@binghamton.edu
B. Davaji
Electrical and Computer Engineering
Northeastern University
360 Huntington Ave, Boston, MA 02115, USA

The ORCID identification number(s) for the author(s) of this article can be found under https://doi.org/10.1002/smll.202304591

DOI: 10.1002/smll.202304591

The common methods used for motion sensing are capacitive, electromagnetic, piezoelectric, electret, and triboelectric sensing. In capacitive sensors, the motion of a movable electrode relative to a fixed electrode changes the system capacitance with a constant applied voltage. Capacitive sensing is featured in microphones, accelerometers, ultrasonic transducers, artificial skin, and in wearable devices.[4-9] In electromagnetic motion sensing, the voltage is produced from a conductor in motion within an electromagnetic field, which is correlated to the motion velocity. Sensing motion with piezoresistive materials benefits from the change in their nominal resistance. This property is used to create vibration sensors from materials such as PDMS-graphene^[10] or a doped silicon layer in MEMS applications.[11,12] Motion sensing with piezoelectric materials occurs by directly producing voltages as a response to strain. Piezoelectricity is featured in microphones, motion alarms, and wearable electronics.[13-16] The electret motion sensors are self-powered capacitive sensors where the bias voltage is replaced with a

charged dielectric (electret polymer) coated on one of the conductors. This type of sensing is used in applications such as wearable sensors, motion detection, and pressure sensing. [17–19] Although the electret motion sensing is self-powered, the charged electrode is dissipated with relatively short periods of time which is why the search continue for more reliable transducers.

The literature review of a recent study demonstrated that the most common self-powered motion sensors use triboelectric transducers, which has been used since 2012 for powering electronics.^[20] The triboelectric transducers exploit the affinity of a material to gain or lose electrons when rubbed by another material; their designs differ in shape and materials used come in pairs such as the liquid metal combination of gallium-indium,^[21] aluminum-teflon,[22] and copper-polyimide.[23] When the triboelectric pair have a bigger difference in electron affinity, more output voltage is produced upon contact or friction between the pair. Triboelectric transducers are used as load sensors, [24,25] wearable devices and artificial skin.^[26] The development of modern sensors comes in parallel with the rise of the Internet of Things that has high energy requirement due to the incorporation of billions of sensors in the network. Research suggests triboelectric generators can provide the power required by some pressure and motion

16136829, 0, Downloaded from https://onlinelibrary.wiley.com/doi/10.1002/smll.202304591 by Test, Wiley Online Library on [02/11/2023]. See the Terms and Conditions (https://onlinelibrary.wiley.com/terms-and-conditions) on Wiley Online Library for rules of use; OA articles are governed by the applicable Creative Commons Licenses

sensors which can address some of the power demand. Triboelectric transducers have many advantages such as bio-compatibility, fabrication simplicity, and high output power density.

Triboelectric generators reached the microscale by incorporating the UV-LIGA process as designed and fabricated by Hamid et al. [12,27] Their design uses Teflon and aluminum as the triboelectric pair and a photo-definable polyimide for a sacrificial layer that is essential for gap creation. Previously, we fabricated a MEMS triboelectric generator in a cleanroom with sputtered aluminum films for conductive layers, polyimide as the dielectric layer, and silicon dioxide for the sacrificial layer, and we used amorphous silicon for a proof mass. [28] The device was used to actuate a MEMS electrostatic switch in the dynamic pull-in range. [29]

Particularly for the purpose of detection, MEMS vibration sensors are required to operate in a wide range of frequencies. Commercial Analog Devices MEMS accelerometers measure up to, for example, 23 kHz in ADXL 1005, 24 kHz in ADXL1004 or 15 kHz in ADXL1003. The analysis of the response at the highfrequency spectrum of the measurements gives useful information for machinery condition-monitoring, test and measurement, acoustic emissions and predictive maintenance. In addition, TENG can be considered as a voltage source when exposed to mechanical vibrations and can drive MEMS switches to indicate a threshold has reached. [29,30] In our previous work, [29] we have shown the conversion of the kinetic energy to a voltage signal for the actuation of the MEMS contact switch in the dynamic pull-in range to detect threshold vibration frequencies or amplitudes. The same device was used as a self-powered accelerometer by applying sinusoidal excitation from 2–10 g at frequencies from 100 to 7000 Hz. $^{[30]}$ We reported a maximum output for the 2 mm \times 2 mm device of 0.7 V, a sensitivity of measurement 70 mV g⁻¹, and a signal-to-noise ratio of 23 dB. The fabrication used springs for stress relief and to enable out-of-plane motion for the top layer of the triboelectric generator. However, film stresses are not necessarily uniform across the wafer and could be a major contributor to failure after release. Their device underwent testing under standard atmospheric conditions and at room temperature. The test outcomes also revealed a shift in the natural frequency and a drop in the generated voltage in response to the reduction in relative humidity from 40% down to 15%.

The study introduces an event-driven MEMS motion sensor with a natural frequency of 4 kHz and high sensitivity (250 mV $\rm g^{-1}$). These qualities make it ideal for a self-powered MEMS microphone. Unlike conventional capacitive-based MEMS microphones needing external bias voltage and amplification circuits, this device overcomes energy source limitations for enhanced performance and cost reduction. The study aims to leverage these findings to develop a high-performance, self-powered MEMS microphone with improved noise performance.

In this work, we take advantage of non-uniform film stress of a warped MEMS-TENG diaphragm to increase the voltage output and improve the sensitivity and signal-to-noise ratio. A failure of the springs results in a direct stiction of the diaphragm to the dielectric layer creating a domed structure, which increases the initial capacitance gap and produces a larger output when it receives a base excitation. Considering the triboelectric effect as a tool for vibration detection, linearity and nonlinearity in electrical output generation are then analyzed. We provide a deep analysis of the theoretical model to understand the underlying physics, which can be used to further optimize the device for a better performance. Finally, the effectiveness of triboelectric vibration sensing in micro and meso scale is compared through analytical results.

This paper continues with Section 2 where mechanism description and modeling are presented. Section 3 is the results and discussion for mechanical and electrical analysis and presents the experimental and analytical results. We conclude the paper in Section 4.

2. Mechanism Description and Modeling

The design of the top layer is inspired by the design of a MEMS accelerometer where the movable electrode is suspended with serpentine springs.^[5] The fabrication of the MEMS triboelectric generator used in this paper is described in ref. [28]. The fabrication process was carried out inside a MEMS fabrication facility. Bottom layer was fabricated with sputtering chromealuminum layer which is etched by inductive-conductive-plasma machine. The polyimide precursor was spun, baked, and etched with reactive-ion-etching. The gap was created by a thin 2 µm film of silicon oxide deposited using plasma-enhanced-physicalvapor-deposition (PECVD). The top layer was formed by sputtering chrome-aluminum and depositing a PECVD film of amorphous silicon. Top layer has a pattern of thin wires forming the springs on the TENG corners with the smallest dimension being 15 µm and the top electrode has release holes with 10 µm diameter. The fabrication is finalized by releasing the structure with vapor HF and the subsequently the stresses causes the top layer to warp. Using an optical profilometer, the surface topology of the warped diaphragm is measured (Figure 1a). This MEMS-TENG has been exposed to severe vibrations as a result of which, the . An optical image from the top view shows the overall outline of the MEMS-TENG (Figure 1b). The surface of the MEMS-TENG is perforated to maximize the exposed area of the sacrificial layer (silicon oxide) to reduce the total time needed for its removal. The colors vary in Figure 1c to illustrate the warped diaphragm surface. All of the springs are damaged and the diaphragm adheres to the polyimide layer along its periphery at two opposite corners (Figure 1d). The rest of the plate is free to move with the new boundary conditions. Using 10× magnification and stitching nine adjacent areas, the whole MEMS-TENG image is captured as shown in this result. There are several scratches on the sensor diaphragm. They look darker because of the large height difference. An optical profilometer was used to make Figures 1d-f. In Figure 1e, the varied topography is shown by changes in the height of four lines, which is reported in µm. The line colors, shown in Figure 1d, show the lines' paths at which the measurements were made with the darkest blue serving as a reference point. The cold and warm color spectrum indicate the lower and larger heights, respectively. The entire surface of the now-warped diaphragm does not adhere to the polyimide substrate, and the unattached part can move in response to vibrations. The adhered part constrains the unattached part within specific boundaries and creates a new resonator with a different effective mass and stiffness from the original flat diaphragm previously reported. [28] The fixed boundaries are thicker at the top left and bottom right. The movable part is similar to a

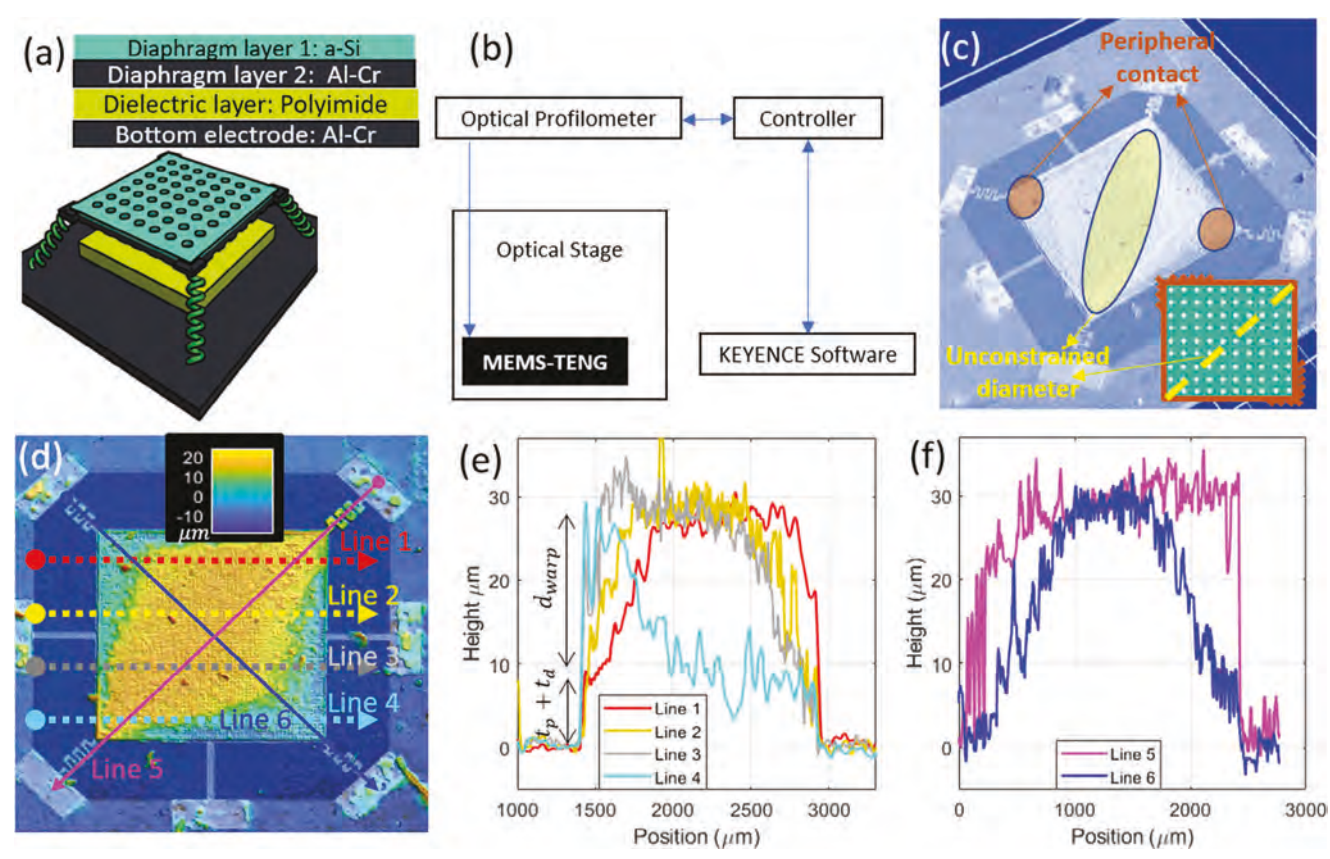


Figure 1. a) The MEMS-TENG in the original state before damage. b) Optical profilometer KEYENCE VK-X1000 LASER MICROSCOPE. c) The optical image from an isometric view showing the warped diaphragm after damage. The colorbar indicates the measured values in µm. d) The optical image from the top view. The horizontal lines 1,2,3, and 4 and the diagonal lines 5, and 6 are used for measuring the topology of the damaged diaphragm. e) Deformation versus the horizontal position of lines 1,2,3, and 4. f) Deformation versus the horizontal position of the diagonal lines 5, and 6.

rhombus. The new constraints make the remained movable part lighter in weight but stiffer in compliance in comparison with four-spring suspended system. Part of the movable electrode to its bottom fixed insulating layer causes different mechanical behavior and demands a new characterization. Experimental analysis for the mechanical characterization of the warped MEMS-TENG is presented below. Using the optical profilometer, the height differences can be graphed along an arbitrary line. The red, yellow, gray, and cyan horizontal lines shown in Figure 2d are used to track changes in the diaphragm's topography, and Figure 1e shows how the once-flat surface has been transformed into an irregularly shaped dome. By setting the base height at 0 on the substrate's surface, the laser profile analysis tool can show the details of the transformation, Figure 1e,f. The tool indicated line 1 started at a height of 7.8 m. However, that result differs slightly from a simple calculation of where the initial height should be. The sum of the substrate Al/Cr, polyimide, the adhered diaphragm including the dimples, the diaphragm Al/Cr, and the amorphous silicon layer $(0.2 \, \mu\text{m} + 5 \, \mu\text{m} + 1 \, \mu\text{m} + 0.1 \, \mu\text{m})$ $+ 1 \mu m$) equals 7.3 μm . Despite the difference (0.5 μm) between the measured and calculated values, we can say with a good approximation that the diaphragm is stuck to the polyimide at two opposite corners. Line 2 indicates that the left side of the diaphragm is very close to the polyimide and starts rising until it approaches the center. Then it starts falling as line 2 ends to the right. According to the variation of height in lines 3 and 4 the domed diaphragm shape is similar to a hovering rhombus. More can be found about the symmetry of the warped diaphragm by looking at the height variation along the diameters. Line 5 shows that this diameter is has more constant height while line 6 indicates the new attached boundary condition which is caused by the stiction of some diaphragm dimples to the polyimide surface. By contrast with the original boundary conditions, the curled-up diaphragm is fixed with direct stiction to its bottom layer as shown in Figure 1f.

The flat diaphragm suspended above the polyimide (Figure 2a) is designed to move up and down (Figure 2b,c) where the serpentines and diaphragm are deflected during external vibrations. The optical measurement provides the geometric information for visualizing the peripheral constraints and warped diaphragm. Using 3ds MAX, the MEMS-TENG is modeled and demonstrated in Figure 2d–f. The diaphragm initially acquires a curled-up equilibrium position. The arched shape of the diaphragm results in a nonlinear mechanical stiffness which allows for a large range of motion toward the substrate and a small span upward (Figure 2d). One can consider this position analogous to an arched doubly constrained plate shown in Figure 2d. During the motion toward the polyimide, the motion downward causes the middle of the diaphragm to curl down (Figure 2e). The constrained diameter of the diaphragm seems to buckle down as

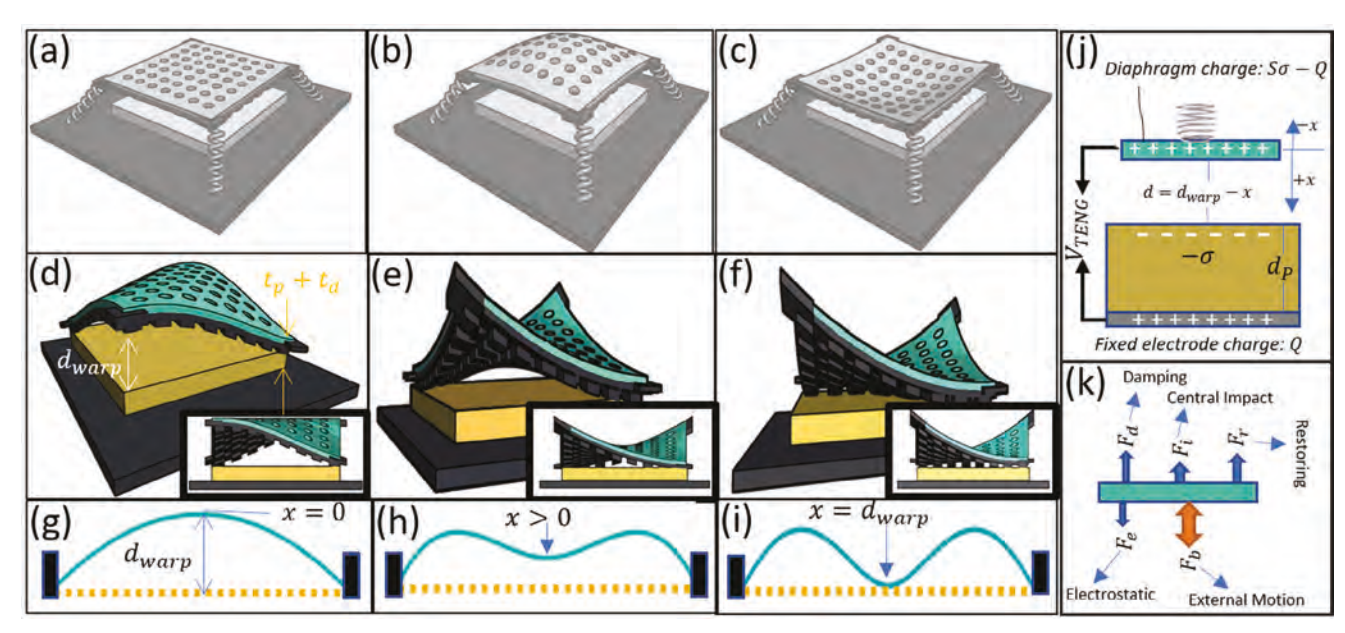


Figure 2. a) MEMS-TENG in its original state. b,c) The undamaged MEMS-TENG in CS mode in the presence of external downward and upward forces, respectively. d,e) Isometric view of warped MEMS-TENG schematic in the first and second stable position, respectively. f) warped diaphragm during contact-separation between the diaphragm center and polyimide. g–i) Analogy between the warped diaphragm and a MEMS bridge in (d–f) with fixed boundaries at two corners, respectively. j) Simplified spring-mass schematic of the MEMS-TENG. k) Free body diagram of the MEMS-TENG movable electrode.

in Figure 2h. During the motion from the initial position to the position of Figure 2e the boundaries in contact are prone to friction forces and consequently, a charge density appears on the polyimide (dielectric) because of triboelectrification. When the g-level of the vibration is large enough, the downward motion of the diaphragm experiences an impact between the diaphragm central area and the polyimide layer (Figure 2i). In this position, the maximum contact area occurs between the triboelectric layers and therefore the largest charge density takes over the dielectric surface.

The model of the MEMS-TENG before damage with operable serpentines (Figure 2a–c) was simplified to a spring-mass-damper with electrostatic force and base-excitation force. The charge density was also considered constant during the vibrations. Because of the significance of the first transverse mode of motion compared to higher modes, the model of the warped MEMS-TENG is simplified to a spring–mass-damper model as indicated in Figure 2j. A model that takes into consideration the special structure of the warped diaphragm needs to consider the nonlinear stiffness as observed in refs. [31, 32].

The mechanics of the device includes a damping force $F_{\rm d}$, restoring force $F_{\rm r}$, electrostatic force $F_{\rm e}$, impact $F_{\rm i}$, and eventually the base-excitation force $F_{\rm base}$ of the external vibration as drawn in the free body diagram Figure 2k. The dynamic equation of the warped MEMS-TENG is:

$$m\ddot{x}(t) = F_{\rm r} + F_{\rm d} + F_{\rm e} + F_{\rm b} + F_{\rm i}$$
 (1)

where x(t) denotes the displacement of the MEMS-TENG center from the initial state Figure 2d, and m is the equivalent mass in Equation (1). Considering the MEMS-TENG position in Figure 2d as the initial position of the diaphragm, in the pres-

ence of a harmonic external vibration, the diaphragm displacement toward the substrate is greater than the motion away from it. The nonlinear phenomenon is represented by a cubic term in the equation of motion as:

$$F_r = -k_1 x(t) - k_2 x^3(t) (2)$$

where k_1 and k_2 are the linear and nonlinear stiffness coefficients in Equation (2). The general idea of inertial sensors is the inertial force as a result of the external vibration, which is:

$$F_b = -ma_{\text{base}}(t) \tag{3}$$

where $a_{\rm base}(t)$ is the base-excitation in Equation (3). The squeezed-film-damping and the structural damping from the contact in the peripheral boundaries of the warped diaphragm resists the motion as demonstrated in the magnified boxes of Figure 6b. A common damping coefficient represents both forces is presented as:

$$F_{\rm d} = -c_{\rm eq} \dot{x}(t) \tag{4}$$

where $c_{\rm eq}$ is the equivalent damping coefficient in Equation (4). During the contact between the diaphragm center and polyimide layer, the surface interactions appear as an adhesion force. The adhesion is modeled as a damping force proportional to the velocity of the diaphragm during contact. A strong linear stiffness correlates with the impact between the triboelectric layers. Because the adhesion force and the surface reaction from the impact create the kinetics during central contact, they are introduced together in the literature as:

$$F_i = -c_i \dot{x}(t) - k_i x(t) \tag{5}$$

(6136829, 0, Downloaded from https://onlinelibrary.wiley.com/doi/10.1002/smll.202304591 by Test, Wiley Online Library on [02/11/2023]. See the Terms and Conditions (https://onlinelibrary.wiley.com/terms-and-conditions) on Wiley Online Library for rules of use; OA articles are governed by the applicable Creative Commons. Licenses

where c_i and k_i are the adhesion force coefficient and impact force coefficient, respectively in Equation (5). The last force is related to the electrostatic force and the charge generation. The accumulated charge on the electrodes (Q(t)) creates an attractive force:

$$F_{\rm e} = \frac{Q^2(t)}{2\epsilon_0 A} \tag{6}$$

where ϵ_0 is the vacuum permittivity which is considered $\approx 8.85 \times$ $10^{-12} \mathrm{Fm^{-1}}$, and A is the effective surface engaged in the electrostatic field in Equation (6). The potential difference between the diaphragm and the bottom Al/Cr is a result of two electrostatic fields; one in the air gap between the warped diaphragm and polyimide layer, and the other is inside the polyimide layer. Charge transfer occurs because of the diaphragm displacement above the charged polyimide (σ_t) and creates a voltage signal (V_{TENG}).^[35]

$$V_{\text{TENG}} = R\dot{Q}(t) = -\frac{Q(t)}{\epsilon_0 A} \left(d(t) + \frac{t_p}{\epsilon_r} \right) + \frac{\sigma_t}{\epsilon_0} d(t)$$
 (7)

where $d(t) = d_{warp} - x(t)$ is the distance between the triboelectric pair, and R is the internal resistance of the MEMS-TENG. $t_{\rm p}$ and $\epsilon_{\rm p}$ are the polyimide thickness and permittivity coefficient, respectively. Triboelectric generators operating in contact-separation mode distribute a charge density on the dielectric surface and the charge density remains nearly constant until the next impact, [36] while a MEMS-TENG with peripheral contact boundaries takes advantage of permanent contact between the diaphragm and the polyimide. The periodic penetration of the diaphragm dimples at the adhered boundaries reinforces the charge generation during the contact-separation at the diaphragm center.[36]

$$\sigma_{t} = \sigma_{0} + \sigma_{p}(a_{\text{base}}) \tag{8}$$

where the total charge density σ_{t} in Equation (8) is made up of a constant value σ_0 and a variable term σ_p as a result of the peripheral contact.

3. Results and Discussion

The characterization of a MEMS inertial sensor consists of the analysis of mechanical properties and electrical output. In mechanical analysis, our first goal is to collect information about the shape of the warped diaphragm where a the MEMS-TENG is actuated by an AC voltage signal between the electrodes. Amplitude of actuation at different spots of the diaphragm can verify the optical profilometry results presented in the previous chapter. Second goal is collecting information about the vibration mode that the system is operating in during the external vibrations. The power spectrum of the vibrometer measurements will help us learn about the operation mode of the diaphragm in transverse direction. The electrical output of such sensors is a potential difference that is an indicator of the external motion. The analysis is followed by the electrical output, including the signal amplitude, g-level range of operation, frequency bandwidth, noise level and signal-to-noise ratio, and eventually, the generated signal quality. The output is measured in the presence of different g-levels and frequencies. The obtained results are used to calculate the sensitivity, frequency response, and the g-level range of operation. The measurements are continued to obtain the noise level, signal quality and signal-to-noise-ratio. Last part of measurements takes a closer look at the quality of the generated signal shape in mechanical-to-electrical transduction of the diaphragm motion.

An electrodynamic shaker B&K 4809 is used for generating the external vibrations. The potential difference V_{TENG} between the two movable and fixed electrodes (see Figure 2d) is measured using a National Instruments 6366 USB data-acquisition system. This device contains 8 inputs that can sense and tolerate $\pm 10 \text{ V}$. The input impedance between the terminals is reported as 100 pF in the data sheet.

The mechanical characterization of a motion sensor is the analysis of the diaphragm motion. We used a laser Doppler velocimetry (LDV) for MEMS motion analysis. Electrodynamic shakers convert electrical energy to mechanical motion which simulates the vibration of moving objects. However, by contrast with mesoscale devices, MEMS devices are an order of magnitude smaller, which means the external vibrations are dominant and MEMS device vibration cannot be measured directly with LDV specially with a single-laser. The MEMS-TENG mechanism depicted in Figure 1a consists of two conductive Al/Cr electrodes, one movable (diaphragm) and one fixed on the substrate. A microscale movable electrode can be driven using capacitive actuation that applies a potential difference between a movable and fixed electrode to generate motion. We used capacitive (electrostatic) actuation instead of an electrodynamic shaker for mechanical characterization where the MEMS movable electrode is measured directly under the laser using LDV (see Figure 4a). Regarding the presented MEMS-TENG in this work, the characterization process is exhibited in **Figure 3**.

3.1. Mechanical Properties

Presented below is the first part of the characterization process for MEMS-TENG. To determine the features of motion sensors, such as frequency response, operation bandwidth, operat-

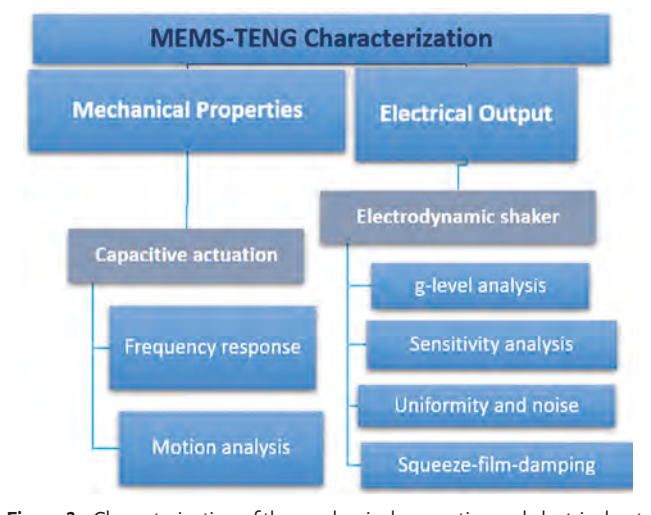


Figure 3. Characterization of the mechanical properties and electrical outputs of the MEMS-TENG.

6136829, 0, Downloaded from https://onlinelibrary.wiley.com/doi/10.1002/sml1.202304591 by Test, Wiley Online Library on [02/11/2023]. See the Terms and Conditions (https://onlinelibrary.wiley.com/terms-and-conditions) on Wiley Online Library for rules of use; OA articles are governed by the applicable Creative Commons License

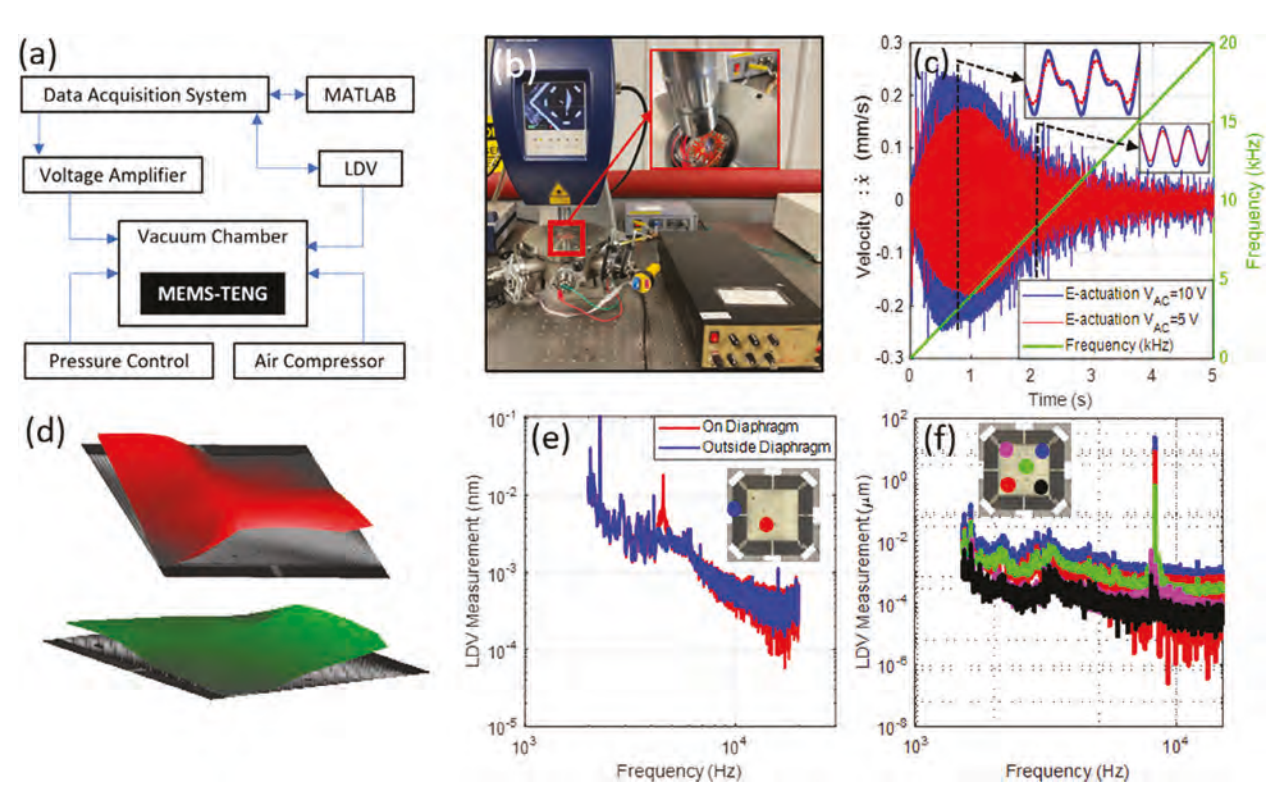


Figure 4. a) Measurement procedure. b) Experimental set-up for the electrostatic actuation of the MEMS-TENG diaphragm. The red arrow points to the magnified MEMS-TENG inside the vacuum chamber. c) Time history of the electrostatic force frequency sweep (forward) with $V_{AC} = 5 \text{ V}$ (red) and $V_{AC} = 5 \text{ V}$ 10 V (blue). d) LDV scanning. 3D images are captured in 8 kHz. e) FFT of the LDV output for the analysis of noise and mechanical natural frequencies. Measurements are conducted in the presence of no external load while the laser is set on the diaphragm and on the fixed substrate. f) FFT of the LDV. The diaphragm was actuated by the capacitive force generated in the presence of $V_{AC} = 5 \text{ V}$ and f = 8 kHz.

ing range of motion, and the quality factor (Q), it is necessary to conduct experimental and analytical investigations. However, because of the complex warped geometry and the damaged springs, modeling the generator as a continuous mechanical system using methods such as finite-element (FE) discretization would require a large computational effort. Instead, we rely on the experimental results and a lumped-mass analytical model to perform the characterization. The goal of this analysis is to determine and verify the natural frequency and real gap between the center of the diaphragm and the polyimide, which are essential parameters for the analysis of triboelectric sensors in contactseparation mode.

For electrostatic actuation, the top and bottom electrodes are connected to the input voltage that is generated in the computer, sent to the DAQ, and transferred to the voltage amplifier. The input signal is governed as:

$$V_{\rm F}(t) = V_{\rm AC} \sin(2\pi f t) \tag{9}$$

where V_{AC} and $V_{E}(t)$ represent the AC voltage amplitude and the electrostatic actuation input, respectively. To observe the MEMS-TENG diaphragm motion in the presence of weak vibrations that do not initiate contact and separation, two input amplitudes of $V_{\rm AC} = 5\,{\rm V}$ and $V_{\rm AC} = 10\,{\rm V}$ are considered. A procedure for the electrostatic actuation of the MEMS-TENG is indicated in Figure 4a. More in-depth testing information is available in Section 5. The frequency is swept from 0 to 20 kHz with the rate of 4 kHzs⁻¹ for 5 s. As described in Figure 4b, using the LDV, the velocity of the MEMS-TENG diaphragm is measured and shown on the left axis of Figure 4c at $V_{\rm AC}$ = 5 V (red) and $V_{\rm AC}$ = 10 V (blue). On the right axis, the frequency of the input is shown. Considering the low voltage input, the velocity magnitude is maximum at 4 kHz which indicates the first natural frequency of the diaphragm. The maximum velocity reaches 0.17 mms⁻¹. This experiment shows that the dominant mode of the resonator after becoming warped is related to the transverse out-of-plane motion at f < 20 kHz. The response at $\,V_{\rm AC}$ = 10 V reaches 0.22 to 0.25 mms⁻¹ at f < 5 kHz. The magnified view of the time history in the resonance region is plotted in the subplots where at f =4 kHz. The velocity signal shape indicates that for a portion of period time, the diaphragm responds to the 10 V input by hitting the polyimide and staying there ($\dot{x} = 0$). The shape of the periodic response is different from the sine shape in this region for the 10 V actuation. Then the diaphragm detaches and continues the rest of the oscillation. While responding to the 5 V, the diaphragm center also hits the polyimide, but does not stick and continues the oscillation after some velocity reduction. As a consequence, the stronger force causes more penetration between the triboelectric layers and longer adhesion time.

Figure 4d shows the LDV scanning mode utilized for the analysis of the diaphragm shape during operation. 3D images are captured in 8 kHz. As shown, at the top of the stroke, the diaphragm verifies the optical analysis reported in Figure 1c. The FFT of the LDV measurements contain some random and non-random

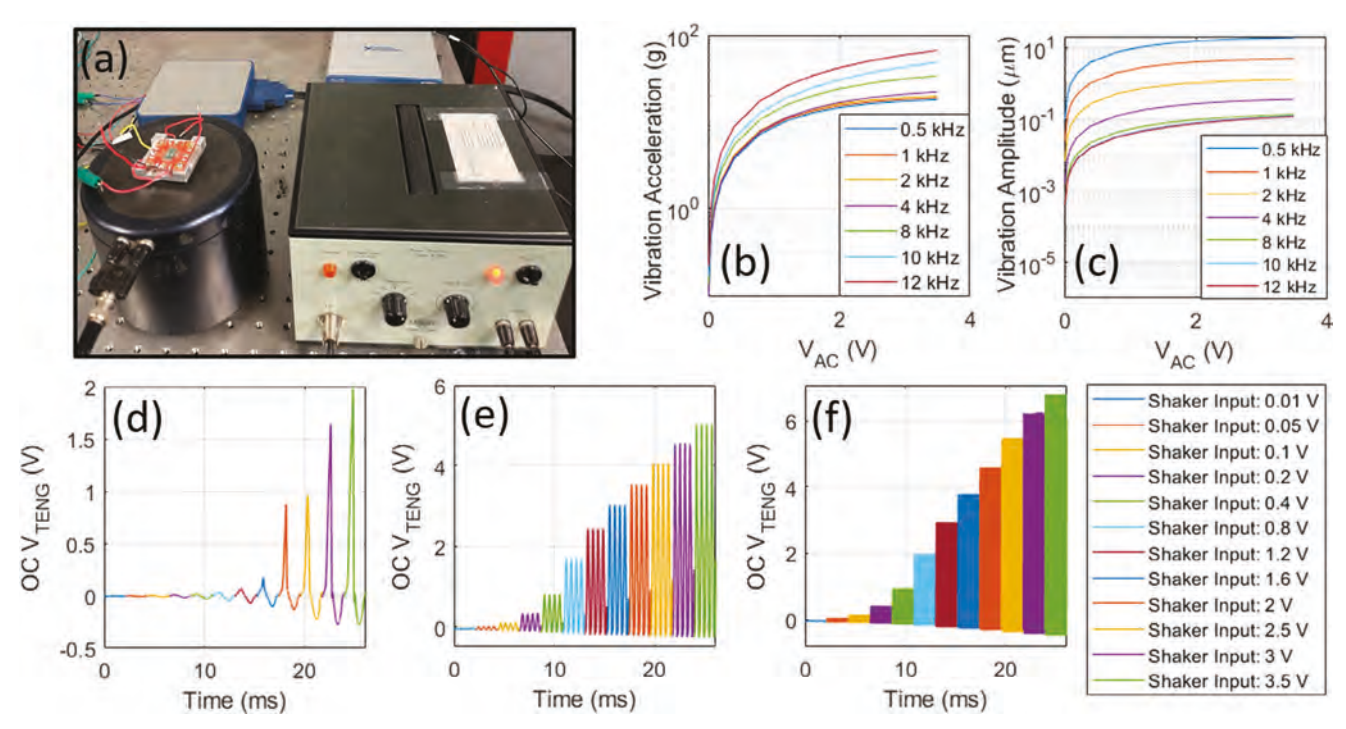


Figure 5. a) Testing setup of the MEMS-TENG as a vibration sensor mounted on a 4809 BK electrodynamic shaker. b) g-level generated by 4809 B&K electrodynamic shaker powered by B&K 2706 amplifier as a function of the input voltage $V_{\rm sh}$ at different frequencies. c) Vibration amplitude generation of 4809 BK electrodynamic shaker powered by B&K 2706 amplifier as a function of the input voltage $V_{\rm sh}$ at different frequencies. d) MEMS-TENG output at f = 500 Hz and different shaker inputs. e) MEMS-TENG output at f = 2 kHz and different shaker inputs. The legends indicate the amplifier input voltage $V_{\rm sh}$.

signals mounted on the main laser Doppler signal. For this reason, at zero external load, we measured a spot on the diaphragm (red) and one spot outside the diaphragm (blue) as shown in Figure 4e. The common peaks show the noise and external disturbances, while the peak at $\approx\!4\,\mathrm{kHz}$ shows the natural frequency of the diaphragm fundamental mode. Figure 4f demonstrates FFT of the LDV at different spots. The diaphragm was actuated by the capacitive force generated in the presence of $V_{\mathrm{AC}}=5\,\mathrm{V}$ and $f=8\,\mathrm{kHz}$. The amplitudes confirm the perceived shape of the diaphragm where the black and magenta at the fixed corners move slightly, while the blue, green and red spots are capable of making around 20 $\mu\mathrm{m}$ displacement.

So far, the LDV results of electrostatic actuation of the diaphragm provided useful information about the operation mode of the warped MEMS-TENG in the presence of transverse vibrations as well as the frequency of that mode. Studying the time-history of the diaphragm center provided a better understanding on the diaphragm dynamics during contact-separation. Based-on the mechanical characterization, the section is followed by the analysis of the electrical output.

3.2. Electrical Output

The induced potential difference between the MEMS-TENG electrodes is an indicator of the motion of this sensor. This device is a variable capacitor that is charged and discharged during the oscillation of the diaphragm. The sensor output is associated with the excitation amplitude (g-level), excitation frequency, geometric

shape, and electrical features such as the MEMS-TENG internal capacitance, charge density, and internal resistance. The performance of the motion sensor such as sensitivity, signal-to-noise-ratio, and signal quality can be evaluated using the experimental results in this subsection.

3.2.1. Vibration Frequency and G-Level

The first step is to build up a set-up that simulates the external vibrations and generates the a variety of g-level and frequencies. The input motion is generated using the electrodynamic shaker which is connected to a power amplifier as illustrated in Figure 5a. The command signal is manipulated in MATLAB and sent to the amplifier through the data acquisition system. V_{TENC} between the MEMS-TENG electrodes is measured using the NI 6366 USB data acquisition system. The laser vibrometer is used for the measurement of the shaker stage velocity and calculation of the base acceleration $a_{\rm base}$ in terms of the g-level. Figure 5b shows the characterization of the electrodynamic shaker B&K 4809 where it maps the input of the power amplifier (V_{sh}) to the generated vibration g-level Equation (9). The g-level is a function of the input frequency as shown in the legend box. The MEMS-TENG is mounted on the shaker and the output is measured at various levels of $V_{\rm sh}$. The MEMS-TENG outputs at f = 0.5 kHz, f= 2 kHz, f = 8 kHz are plotted in Figure 7d–f, respectively. Each interval of 2 ms contains a $V_{\rm TENG}$ time-history starting from $V_{\rm sh}$ = 0.01 V to $V_{\rm sh}$ = 3.5 V. The amplifier is limited by $V_{\rm sh}$ = 3.5 V where a red alarm light on the amplifier turns on.

(6136829, 0, Downloaded from https://onlinelibrary.wiley.com/doi/10.1002/smll.202304591 by Test, Wiley Online Library on [02/11/2023]. See the Terms and Conditions (https://onlinelibrary.wiley.com/terms-and-conditions) on Wiley Online Library for rules of use; OA articles are governed by the applicable Creative Commons. Licenses

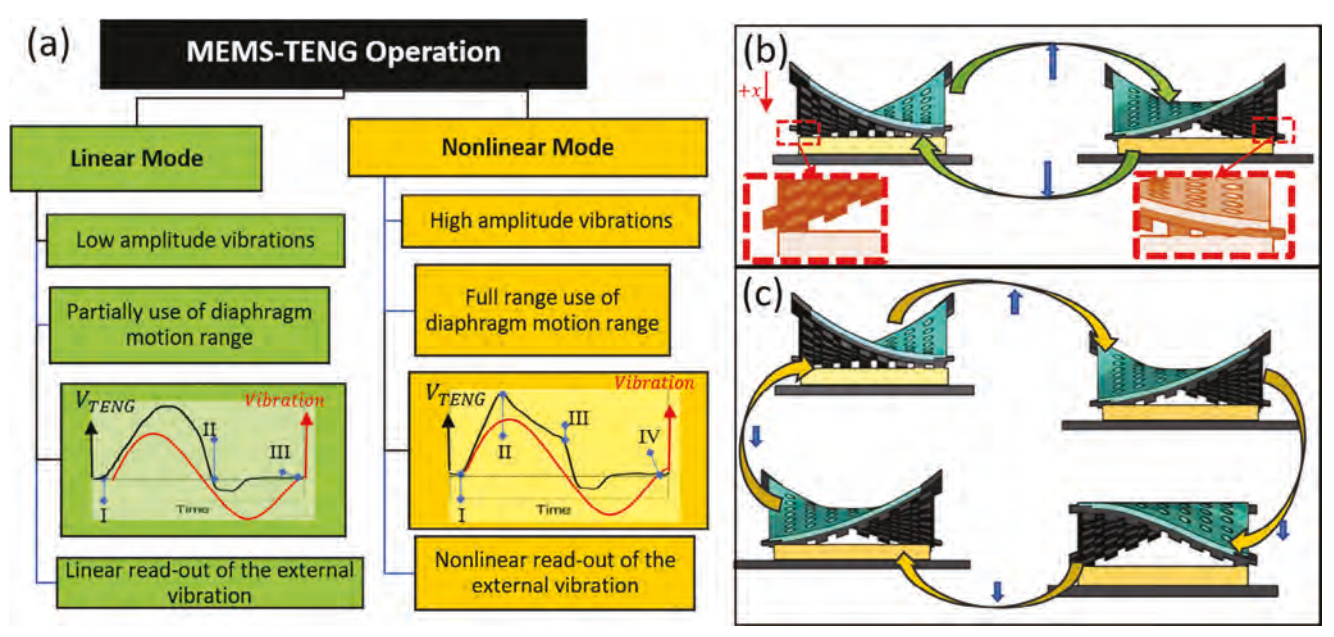


Figure 6. a) Linear and nonlinear modes of a warped MEMS-TENG. b) Schematic of the operation in linear mode (peripheral contact highlighted in the red boxes). c) Schematic of the operation in nonlinear mode.

This part of measurements takes a closer look at the quality of the generated signal shape in mechanical-to-electrical transduction of the diaphragm motion. A deeper investigation of the MEMS-TENG output signal shape is presented in the following. The MEMS-TENG operates in two modes (see Figure 6) as linear and nonlinear. Considering the MEMS-TENG operating at a low g-level (less than 10g at 1 kHz), we begin the process when the diaphragm starts moving upward and peels off from polyimide (I). At this moment, the voltage is zero and the charge on the metal electrodes has been dissipated. However, a charge density exists on the polyimide as a result of the permanent friction between the diaphragm and polyimide at the attached boundaries as well as the instantaneous friction during the contact-separation of the free diagonal. During the diaphragm's upward motion, the voltage signal follows the external vibration until it touches the polyimide again (II). Because of the negative acceleration, the diaphragm center adheres the polyimide between the states II and III. Figure 6b demonstrates the warped MEMS-TENG states during the linear mode.

In the nonlinear regime, the relation between the external vibration and the generated voltage signal shape is mostly nonlinear. The initial state (I) is considered identical to the linear mode. In the presence of vibrations with the g-levels larger than 10g, the diaphragm travels a significantly large distance and causes a large air gap. Subsequently, V_{TENG} decays with a sharp slope state II, and it does not precisely follow the external vibration. When the air gap becomes relatively smaller in state III, V_{TENG} continues to become similar to the external vibration again. The diaphragm adheres to the polyimide during the downward excitation force and decays to $V_{\text{TENG}} = 0 \,\text{V}$ in state IV. Figure 6c shows the dynamics of the warped MEMS-TENG in the presence of external vibration in the nonlinear regime.

The nonlinearity of conversion is considered as an undesired feature in electromechanical transduction. However, there is a trade-off between a nonlinear transduction and becoming event-driven, that is, removing the need for the amplification circuitry, filtering circuitry, and AC/DC input. In the following, the operation at various g-levels and frequencies considering the linear and nonlinear modes of operation is presented.

The MEMS-TENG outputs at a constant frequency and different g-levels are measured as shown in **Figure 7**a–c. At f = 1 kHz, the MEMS-TENG output seems linear at the g-levels less than 10g because the V_{TENG} identically follows the external vibration. At the top, a subplot shows an example of this mode at f = 1 kHz where V_{TENG} (green graph) follows the motion in the presence of harmonic vibrations (red graph). The operation mode switches to the nonlinear mode at the g-levels more than 10g where the center of the diaphragm moves away from the polyimide layer and becomes dome-shaped in a portion of the vibration cycle. As the glevel is increased, the nonlinear decaying portion is extended. For example, the decaying portion is increased from 0.225 to 0.266 ms when the g-level is increased from 15.2g to 18.5g.

When the diaphragm is in the curled-up position, the structure becomes less compliant in the upward direction. During the curled-up situation, the decaying part of the V_{TENG} does not follow the external vibration, and behaves similarly to a discharging capacitor. Interestingly, all the signals in the nonlinear mode in a constant frequency such as 15.2g, 17g, 18.5g, and 19g at 1 kHz follow the same decaying function in the curled-up position. Similarly, the linear and nonlinear modes are observed at f = 4 kHz as in Figure 7b. At g-levels smaller than 18g, the MEMS-TENG operates at the linear mode, and it switches to the nonlinear mode when the g-level exceeds 18g. The nonlinear portion of the generated voltage at 19g, 20g, and 22g mount on the same decaying function (Figure 7f). Increasing the frequency to 12 kHz enables the B&K electrodynamic shaker 4809 to generate g-levels up to 66g. The central contact threshold at this frequency is a measured

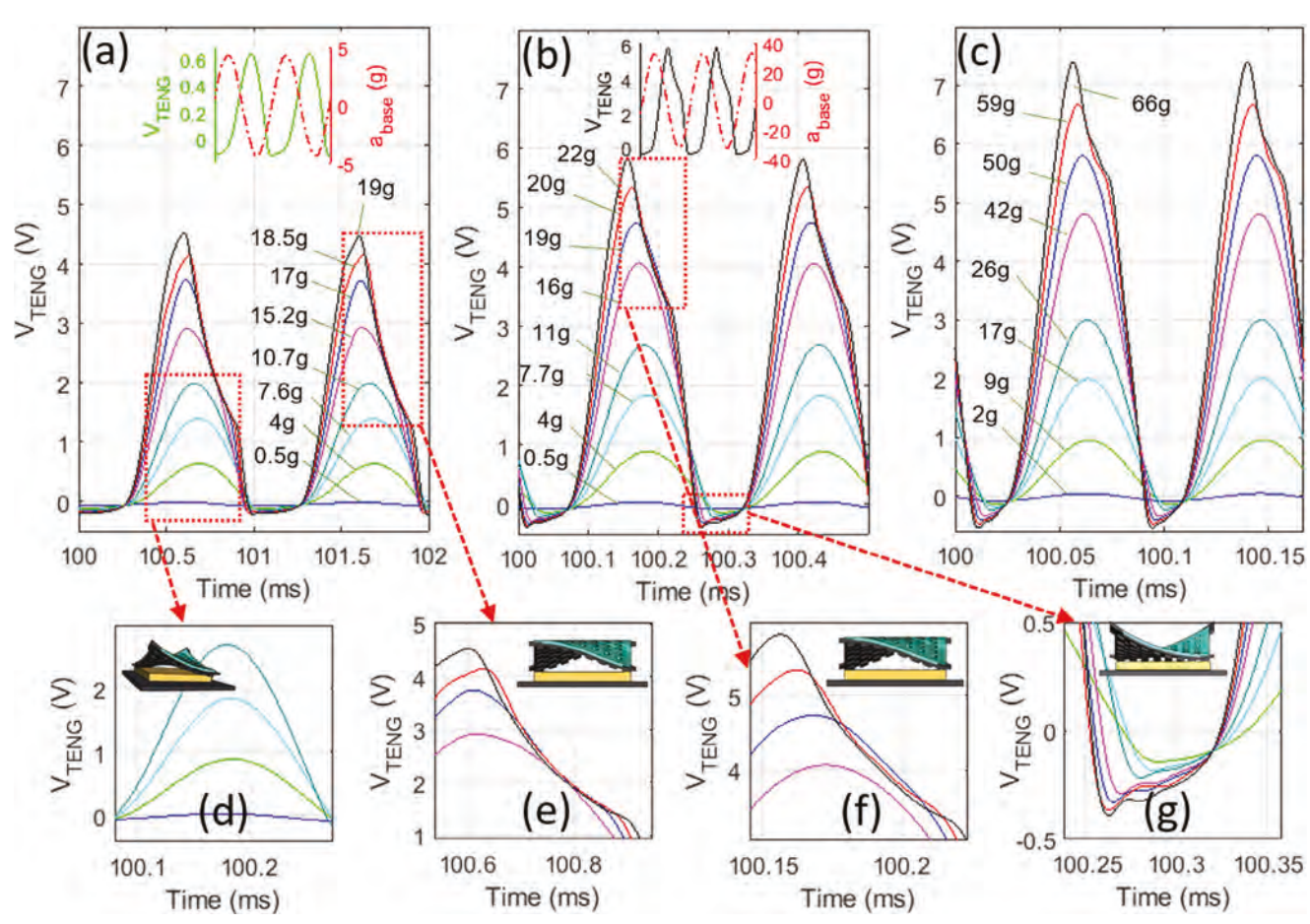


Figure 7. Measured MEMS-TENG output. a) $f = 1 \, \text{kHz}$ and various g-levels. b) $f = 4 \, \text{kHz}$ and various g-levels. c): $f = 12 \, \text{kHz}$ and various g-levels. d) Positive part of the MEMS-TENG output at $f = 1 \, \text{kHz}$ at g-levels smaller than 10g in linear mode. e) Positive part of the MEMS-TENG output at $f = 1 \, \text{kHz}$ at g-levels larger than 10g in nonlinear mode. f) Positive part of the MEMS-TENG output at $f = 4 \, \text{kHz}$ at g-levels larger than 16g in the nonlinear mode. g) Negative part of the MEMS-TENG output at $f = 4 \, \text{kHz}$ during adhesion of the diaphragm center to the polyimide.

50g where $V_{\rm TENG}=5.8\,\rm V$. At higher g-levels the MEMS-TENG operates in nonlinear mode; for example, 7.3 V is generated at 66g. The significant voltage produced at the MEMS scale is seven times larger compared to the state-of-the-art reported in our prior MEMS-TENG study. [30] The increase in the voltage is caused by the increased displacement range of the diaphragm as a result of the dome-shaped structure of the MEMS-TENG and the adhesion of the periphery of the diaphragm to the polyimide. So far, the time-history of MEMS-TENG output in the presence of vibrations with various g-levels and frequencies were provided. The results are used for further analysis on the sensitivity of the device.

3.2.2. Sensitivity

An important part of characterization evaluating the sensor at different g-levels and frequencies. The sensitivity measurement procedure is shown in **Figure 8a**. The measurements are conducted in the 1 to 12 kHz bandwidth. The electrodynamic shaker becomes limited in generating harmonic vibrations becomes as the frequency increases. In the presence of a harmonic base-

excitation, the generated voltage is graphed versus the g-level in Figure 8b. At f = 1 kHz, the generated voltage linearly increases with the g-level for the g-levels smaller than 15g and then starts to behave nonlinearly. At $f = 2 \,\mathrm{kHz}$, the slope of the graph becomes steeper and the nonlinear portion starts at 18g. The slope also increases at f = 4 kHz in the linear range. The larger g-levels are missing for f = 1, 2, and 4 kHz because of the limited bandwidth of the shaker and the power amplifier in generating vibrations. At higher frequencies, the slope starts to decrease. While the maximum V_{TENG} is increased because at higher frequencies, the shaker can generate much larger g-levels. For example, at f= $8 \, \text{kHz}$, the linear slope is $200 \, \text{mVg}^{-1}$ and the maximum generated voltage is $V_{TENG} = 7.3 \text{ V}$ at 34g. The largest frequency that is reported in this work is $f = 12 \,\text{kHz}$ which contains a large linear range of operation, and the generated voltage of 7.3 V at 66g. Because of the limited shaker capability in generating large g-levels at low frequencies, the 3D surface of the generated voltage is partially graphed at lower frequencies. Figure 8b,d simplify the illustration of the variation of MEMS-TENG output because of the g-level and vibration frequency.

One may be interested in studying the vibration sensor performance in the presence of different amplitudes. In addition

16136829, 0, Downloaded from https://onlinelibrary.wiley.com/doi/10.1002/smll.202304591 by Test, Wiley Online Library on [02/1/2023]. See the Terms and Conditions (https://onlinelibrary.wiley.com/terms-and-conditions) on Wiley Online Library for rules of use; OA articles are governed by the applicable Creative Commons Licenses

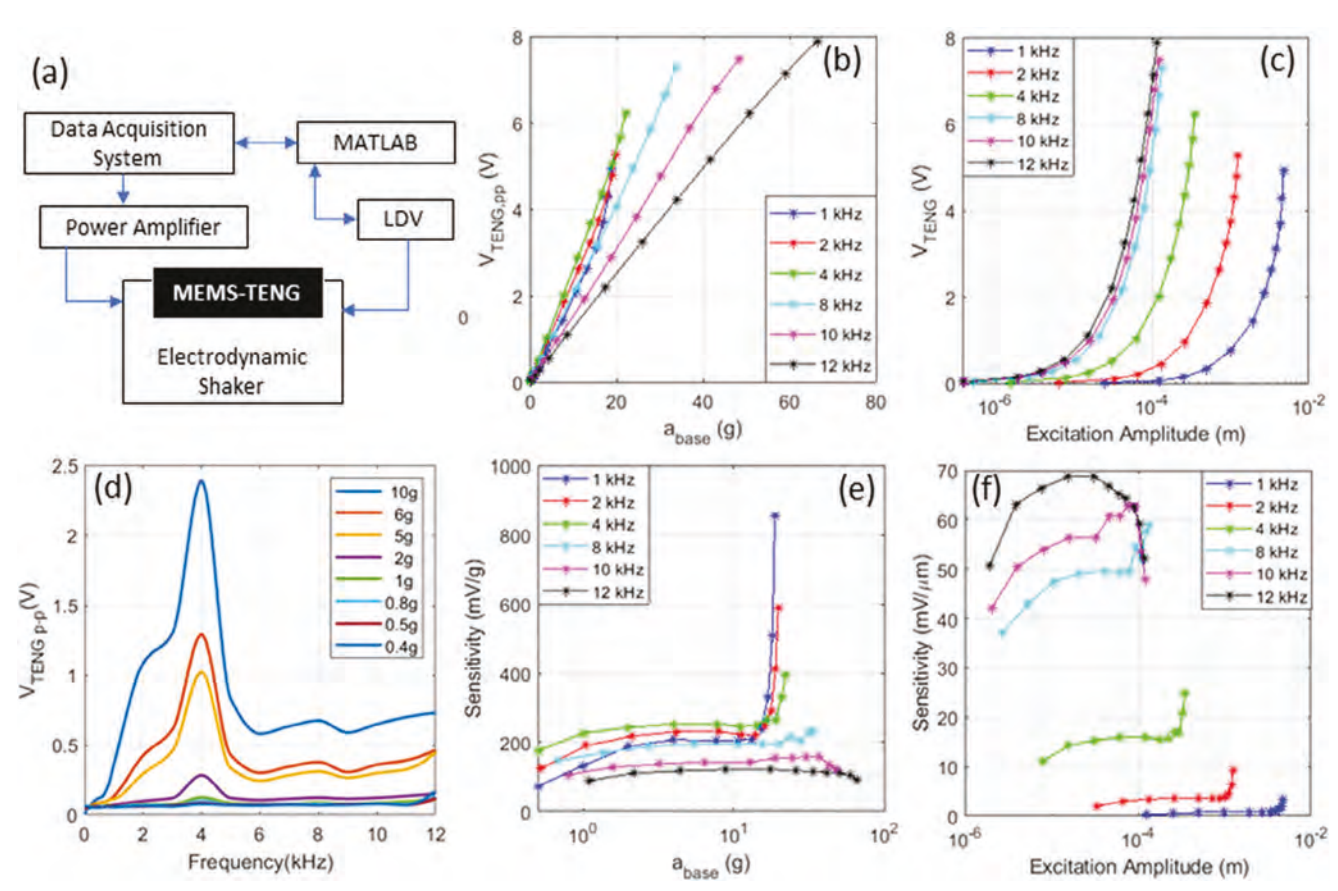


Figure 8. a) Measurement procedure. b) Voltage generation of the MEMS-TENG versus the excitation g-level at different frequencies. c) Open-circuit voltage generation of the MEMS-TENG versus the vibration amplitude at different frequencies. d) Open-circuit voltage generation of the MEMS-TENG versus the vibration frequency at different g-levels. e) The sensitivity of the MEMS-TENG versus base acceleration at different frequencies. f) The sensitivity of the presented MEMS-TENG versus vibration amplitude at different frequencies.

to the g-level of the external vibration, the amplitude of vibration is an important feature to be analyzed. The voltage generation with different base-excitation amplitudes is measured and reported in Figure 8c. The measured MEMS-TENG voltage is illustrated at different excitation amplitudes. The amplitudes of vibrations are determined by experimentally characterizing the relation between input voltages $V_{\rm sh}$ and the measured electrodynamic shaker displacement at different frequencies f. Considering the experimental results, in the presence of a constant excitation amplitude, the MEMS-TENG generates more potential difference at higher frequencies.

Given the infrequent practice of reporting sensor output at constant frequencies and various g-levels, we have incorporated Figure 8d to present the frequency response of the MEMS-TENG output. The findings indicate that when operating at low frequencies, specifically below the natural frequency, the voltage generated remains relatively low. As the frequency increases, it progressively rises until it reaches its zenith at the natural frequency. Beyond this point, a more stable plateau emerges, a characteristic highly sought after in MEMS sensors. Consequently, we have designated this region as the preferred operational bandwidth.

Sensitivity in MEMS sensors is typically expressed as the ratio of the change in the output signal (usually voltage or capacitance) to the change in the input physical quantity (e.g., acceleration, pressure, etc.). For example, if a MEMS accelerometer has a sensitivity of 1 mVg⁻¹, this means that for every 1g change in acceleration, the output voltage of the sensor will change by 1 mV. The slopes of the responses in Figure 8b indicate the sensitivity to the variation of the sensor output against the input change. The sensitivity of the MEMS-TENG is investigated by considering the g-level and frequency of the vibration. Figure 8e indicates how much the output voltage varies in the presence of a g-level change. As expected, the largest sensitivity happens around $f = 4 \,\mathrm{kHz}$ which is close to the first natural frequency of the MEMS-TENG. Then it decreases for higher frequencies up to 12 kHz. Interestingly, the linear operation range where the sensitivity remains constant can be obtained as shown in Figure 8e. The results reveal the sensitivity remains between 150 and $250\,\mathrm{mVg^{-1}}$ in the bandwidth of 1 to $12\,\mathrm{kHz}$. The sensitivity graphs roll off at low g-levels. At $f = 1 \,\mathrm{kHz}$ the roll-off happens at 2g, while this value is improved (smaller roll-off). Using the measured values in Figure 8c, the slope of the graphs provides the sensitivity of the motion sensor to the vibration amplitude at different frequencies, see Figure 8f. Unlike the sensitivity to the g-level, the sensitivity to the vibration amplitude is represented by the unit of mVµm⁻¹. The sensitivity to vibration amplitude is increased monotonically with the frequency increase.

The non-uniform sensitivity at different frequencies is an undesired feature for motion sensors. However, during the characterization of TENG as electromechanical transducer, the input-to-output relation can be obtained by using the characterized data at different frequencies as in Figure 8. The event-driven feature of MEMS-TENG vibration sensing and voltage generation is achieved at the expense of adding post-processing the measured data due to the non-uniform sensitivity.

The presented MEMS TENG was operated at up to 67g with a high frequency such as 500 Hz to 12 kHz. The number of the cycles and the severity of the vibration shows the device in the current position (as shown in Figure 1) is immensely more robust in comparison with the suspended MEMS diaphragm with serpentines on four sides.^[28] Regarding the durability of the presented device, we did not have a chance to conduct a durability test because as explained in the mechanism description section, the film stress caused the warped shape. Governing stress is a tedious task. We did not have numerous fabricated devices with the same curvature for doing the durability test.

For capacitive sensing such as accelerometers and MEMS microphones, the sensitivity remains constant all over the operating bandwidth because the range of motion of the industrial capacitive sensing is very small compared to the gap between electrodes.^[7,13] Consequently, the electrostatic and structural nonlinearities are negligible for the operation range of such sensors. Due to this small motion, one observes a low capacitance change and therefore a low amplitude of output from the capacitive sensors. However, rectification and signal amplification are needed because of low signal amplitudes.

Another key feature of vibration sensors is their signal amplitude compared to the noise level. By using the sensitivity results and measurement of noise-level, signal-to-noise-ratio of the proposed MEMS-TENG is presented in the following.

3.2.3. SNR and Nonuniformity

In the presence of a uniform harmonic base excitation, some non-uniformity may be observed in the electrical output of motion sensors. This phenomenon is usually more significant for the operation at low g-levels where the ratio between the strength of the useful signal and the discrepancy is relatively small. Even in the presence of a uniform continuous external vibration, the background noise appears as an inevitable random instantaneous signal mounted on the sensor output. Micro scale inertial sensors are more likely prone to noises and low SNR because of the minute motion range of micromachined movable electrodes. The SNR of a MEMS sensor depends on various factors, such as geometric design, measurement instruments, the environment, and signal conditioning electronics. SNR can be evaluated by measuring the sensor's output in the presence of noise as well as the noise RMS when the sensor is not operating.

The time history of the MEMS-TENG at different g-levels is shown in Figures 9a-d for 7 ms. The variation of the maximum and minimum of the signals are illustrated with green and red lines, respectively. Considering linear mode, at low baseexcitation, the non-uniformity of the MEMS-TENG output is obvious as the green and red lines vary significantly (Figure 9a). In contrast, at a larger g-level, Figure 9b, the deviation is reduced

because the signal amplitude is relatively larger than the noise floor. Considering the nonlinear mode, Figure 9c,d, at the g-levels of 15g and 22g, the noise effect is much smaller than the linear mode because of the larger signal amplitude. The root mean square deviation (RMSD) is an indicator of the noise effect on the non-uniformity of the measured signal. First, the average of the signal maximums (green line) and minimums (red line) among *N* oscillations is calculated. The maximum and minimum of the ith oscillation are denoted by M_i and m_i , respectively. Then the averages are defined as:

$$\bar{M} = \frac{1}{N} \sum_{i=1}^{N} M_i \tag{10}$$

$$\bar{m} = \frac{1}{N} \sum_{i=1}^{N} m_i \tag{11}$$

where \bar{M} and \bar{m} indicate the averages of the upper and lower bounds of the MEMS-TENG output in Equations (10) and (11). The deviation from the average value [Equations (10) and (11)] is represented by RMSD that is defined as:

$$RMSD_{max} = \sqrt{\frac{\sum_{i=1}^{N} (M_i - \bar{M})^2}{N}}$$
 (12)

$$RMSD_{min} = \sqrt{\frac{\sum_{i=1}^{N} (m_i - \bar{m})^2}{N}}$$
 (13)

where RMSD_{max} and RMSD_{min} denote the RMSD of the signal maximums and minimums in Equations (12) and (13), respectively. We used the discretized definitions for evaluating the nonuniformity of the MEMS-TENG output instead of a continuous integration over oscillation periods because of simplification. We use RMSD to define deviation as a criterion for indicating the non-uniformity where Equations (12) and (13) are summed up and normalized by their average peak-to-peak values \bar{M} and \bar{m}

Deviation =
$$20 \log \left(\frac{\text{RMSD}_{\text{max}} + \text{RMSD}_{\text{min}}}{\bar{M} + \bar{m}} \right)$$
 (14)

Figure 9e shows deviation versus the g-level in dB at different frequencies. In the context of the microfabricated triboelectric device proposed in this work, SNR is defined as the peak-to-peak generated voltage (that is the difference between the \bar{M} and \bar{m}) divided by the maximum noise amplitude within a portion of time history.

At different frequencies, deviation is measured and reported in Figure 9e. At 0.1g, the deviation is at maximum (-40 to -50 dB). Common between all the frequencies, deviation is decreased between 0.1g and 1g and remains at the minimum (-60 to -70 dB) in the range of 1g to 10g. This result indicates the range from 1g to 10g has a more uniform output. The deviation is again increased as the g-level of the external vibration is increased.

In MEMS sensors, SNR is a key performance metric that indicates how accurately a sensor detects and measures motion relative to noise that is measured at the zero force condition.

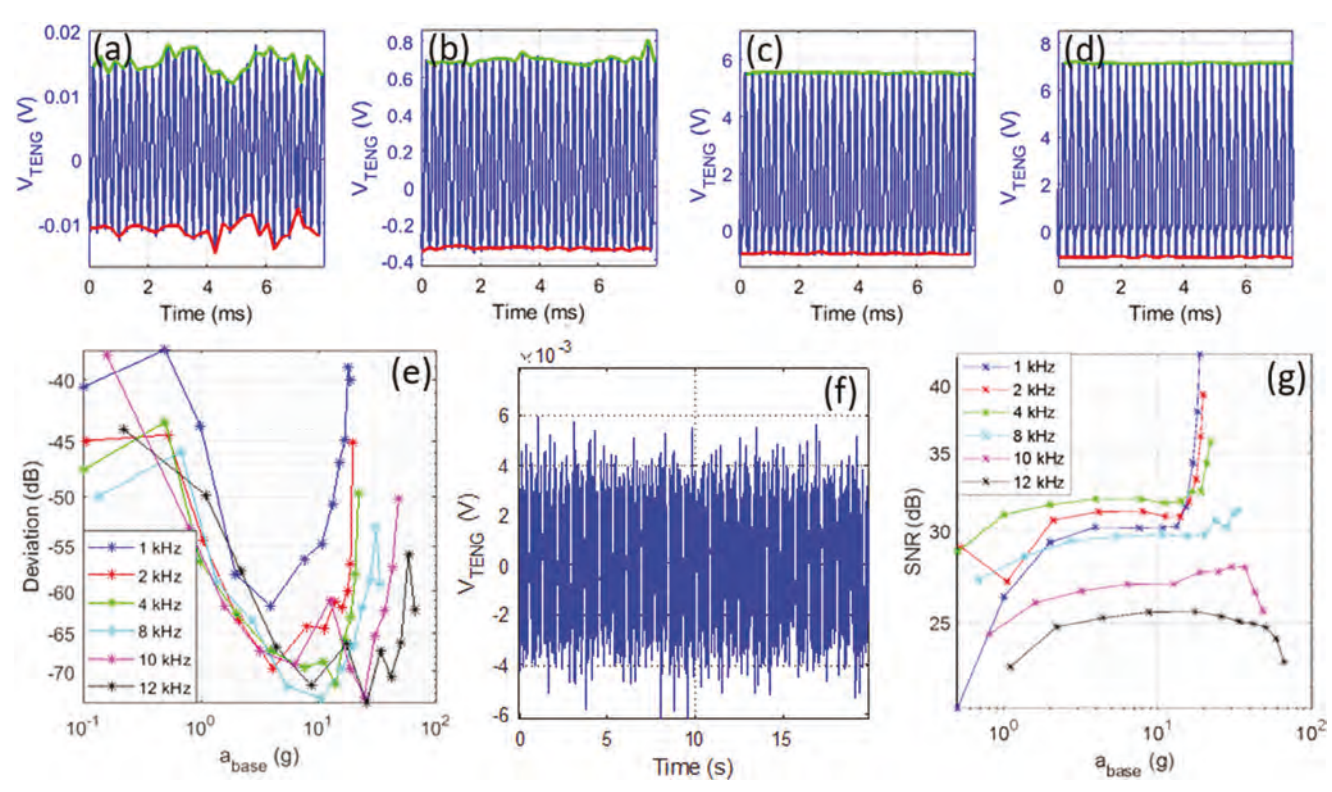


Figure 9. a–d) The MEMS-TENG output in the presence of 4 kHz sinusoidal vibrations with the g-levels of 0.1g, 2g, 15g, and 22g, respectively. The green graphs indicate the upper bound, while the red graphs indicate the lower boundary of the V_{TENG} . e) the standard deviation of the lower bound of the MEMS-TENG output at different frequencies. f) the standard deviation of the upper bound of the MEMS-TENG output at different frequencies and g-levels.

 $V_{\rm TENG}$ was measured for 20 s as shown in Figure 9f with no vibration load. The RMS of the zero-load measurement of 0.0027 V is considered to be the noise level. Therefore, SNR is calculated as the peak-to-peak of the output divided by the noise level.

$$SNR = 20 \log(\frac{Sensitivity}{Noise})$$
 (15)

Figure 9g shows SNR at different frequencies. The maximum SNR is measured 32 dB at $f=4\,\mathrm{kHz}$, which is the natural frequency of the warped diaphragm as demonstrated in the mechanical characterization (Figure 4b). The SNR is drastically increased at the end of the operation range at each frequency, because in that region, the MEMS-TENG generates the maximum voltage that it can make (Figure 8b). At 1 kHz, the SNR is ≈ 30 dB. At high frequencies such as 10 and 12 kHz, the lowest SNR was measured 27 and 25.5 dB, respectively. The measured SNR shows an improvement in the sensor performance as indicated in **Table 2**.

Researchers showed that the surface forces between MEMS components vary at different ambient pressures.^[37] In addition, due to the change of Q-factor, we were curious to know how much air squeeze-film-damping affects the voltage generation. In the following, the results at low pressure are presented.

3.2.4. Effect of Squeeze-Film-Damping

Squeeze-film-damping is a significant dynamic effect that resists the velocity of the movable parts because of the compression of air between movable and fixed parts. The resisting force is a nonlinear function of the air film thickness. In MEMS and NEMS (nanoelectromechanical systems) this effect is remarkable because of the small gaps between the electrodes. Triboelectric nanogenerators in contact-separation mode experience zero-gap position during contact. In particular, MEMS-TENG experiences gaps ranging from a few microns to the zero-gap position. Therefore, it is important to investigate squeeze-film-damping using practical experiments and theoretical analysis. The experimental results discussed earlier in this paper were conducted in the ambient pressure of the atmosphere. We also tested the proposed MEMS-TENG in a near-vacuum (1 Torr). The MEMS-TENG was placed in a vacuum chamber where the pressure was controlled by a vacuum pump and a valve as illustrated on Figure 10a,b. The MEMS-TENG output is measured at different g-levels at 4kHz. The operation in linear and nonlinear modes is shown in Figures 10c,d, respectively. Results depict that the generated voltage is larger in low pressures (dark-colored graphs) compared with the high pressure results (light-colored graphs). The difference could be because squeezed-film-damping is more effective at higher pressures. More damping causes smaller diaphragm motion and smaller $V_{\rm TENG}$. Figure 10e compares the sensor output at low and high pressures. The pressure effect is more

16136829, 0, Downloaded from https://onlinelibrary.wiley.com/doi/10.1002/smll.202304591 by Test, Wiley Online Library on [02/11/2023]. See the Terms and Conditions (https://onlinelibrary.wiley.com/terms-and-conditions) on Wiley Online Library for rules of use; OA article are governed by the applicable Creative Commons Licensee and Conditions (https://onlinelibrary.wiley.com/terms-and-conditions) on Wiley Online Library for rules of use; OA article are governed by the applicable Creative Commons Licensee and Conditions (https://onlinelibrary.wiley.com/terms-and-conditions) on Wiley Online Library for rules of use; OA article are governed by the applicable Creative Commons Licensee and Conditions (https://onlinelibrary.wiley.com/terms-and-conditions) on Wiley Online Library for rules of use; OA article are governed by the applicable Creative Commons Licensee and Conditions (https://onlinelibrary.wiley.com/terms-and-conditions) on Wiley Online Library for rules of use; OA article are governed by the applicable Creative Commons Licensee and Conditions (https://onlinelibrary.wiley.com/terms-and-conditions) on Wiley Online Library for rules of use; OA article are governed by the applicable Creative Commons Licensee and Conditions (https://onlinelibrary.wiley.com/terms-and-conditions) on Wiley Online Library for rules of use; OA article are governed by the applicable Creative Commons Licensee and Conditions (https://onlinelibrary.wiley.com/terms-and-conditions) on the condition of the

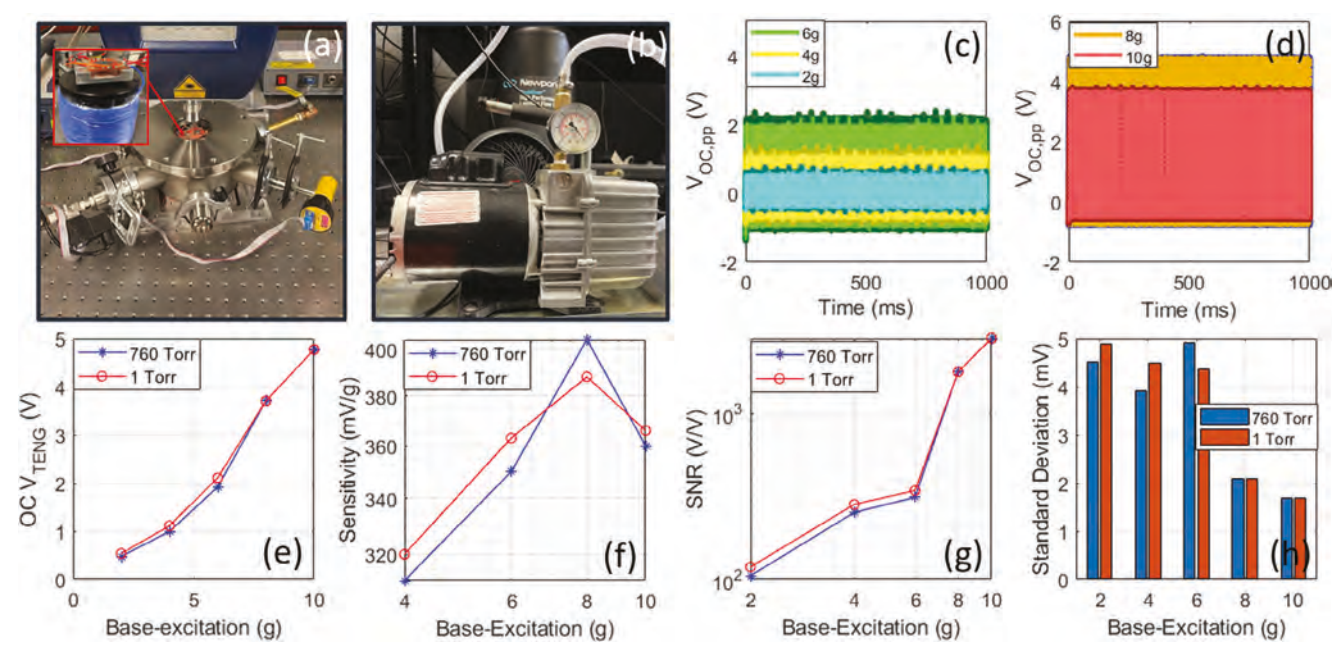


Figure 10. a) Test setup of the MEMS-TENG inside a vacuum chamber. b) gas pump. c) MEMS-TENG operation in the linear mode at the atmosphere (light) and near-vacuum (dark) conditions. d) MEMS-TENG operation in nonlinear mode at the atmosphere and near-vacuum conditions. e) The open-circuit output of the MEMS-TENG at different pressure conditions. f) Sensitivity of the electrical output to the vibration acceleration. g) The effect of ambient pressure on the signal-to-noise ratio of the MEMS-TENG. h) The standard deviations of the open-circuit output of the MEMS-TENG (in mV) at different pressure conditions.

significant in the linear mode where the generated voltage and the noise are smaller. Operation at low pressure provides more sensitivity and a better SNR (Figure 10f,g) because of the larger output. To evaluate the uniformity of the generated voltage, RMSD is evaluated at different g-levels in high and low pressures. At 2g and 4g, the output is more uniform at higher pressures. In contrast, the deviation is more significant at 6g. The deviation difference is negligible in the nonlinear mode (high amplitudes).

3.2.5. Analytical Modeling

To obtain the mechanical and electrical responses of the MEMS-TENG, Equations (1, 7) are solved using ODE45 solver in MAT-LAB where Equation (1) is actuated by the external vibration $F_{\rm b}$ = $m g_{\text{level}} \sin(2\pi f t)$. As in Section 2, the following forces are considered in the mechanical model: base-excitation, structural and squeeze-film damping, restoring force, contact-separation force, and electrostatic force. The effect of mechanical and electrical parameters on the motion of the movable electrode has been an interesting topic for researchers.[38-42] This work introduces new geometric features for MEMS-TENG such as the gap created by the curled diaphragm and fixed boundary conditions instead of serpentine spring support. In this part, using the simulation results, we will delineate the effect of parameters that govern the physics of a microscale TENG device. Considering the mechanical characterization in Section 2, the natural frequency of the warped MEMS-TENG in transverse mode was measured at $f_0 \approx$ 4 kHz. The stiffness of the system is obtained in a way that the generated voltage matches the simulations at 1 kHz and 1g vibration level. Therefore, the linear and nonlinear parts of the structural stiffness are obtained 2.8 N m⁻¹, 3.1×10^{-5} N m⁻³, respectively. In comparison, the nonlinear part does not contribute to the restoring force in comparison with the linear part.

Then, the equivalent mass of the diaphragm is calculated as:

$$m = k_1/(2\pi f_0)^2 = 4.43 \times 10^{-9} \text{ kg}$$
 (16)

The real mass of the MEMS-TENG is calculated as:

$$m_r = \rho_{aSi}.A.t_{aSi} + \rho_{AlCr}.A.t_{AlCr} = 6.02 \times 10^{-9} \text{ kg}$$
 (17)

The densities and thicknesses are available in **Table 1**. The real mass Equation (17) is 25% heavier that the equivalent mass Equation (16). The difference is because not all the points on the continuous system are moving with the same amplitude, which

Table 1. Dimensions of the MEMS-TENG.

| Parameter | Symbol | Value |
|-------------------------------|---------------------|---|
| Side length | 1 | 1500 μm |
| Triboelectric layer thickness | t_{T} | 5 μm |
| Warped gap | d_{warp} | 20 μm |
| Top-electrode thickness | t_1 | 100 nm |
| Proof mass thickness | t_2 | 1 μm |
| Bottom-electrode thickness | t_3 | 200 nm |
| Fundamental frequency | f_0 | 4 kHz |
| Chrome-aluminum density | $ ho_{CrAl}$ | 3455 kgm ⁻³ (17% chrome 83% aluminum) |
| Amorphous silicon density | $ ho_{aSi}$ | 2330 kgm ⁻ 3 |

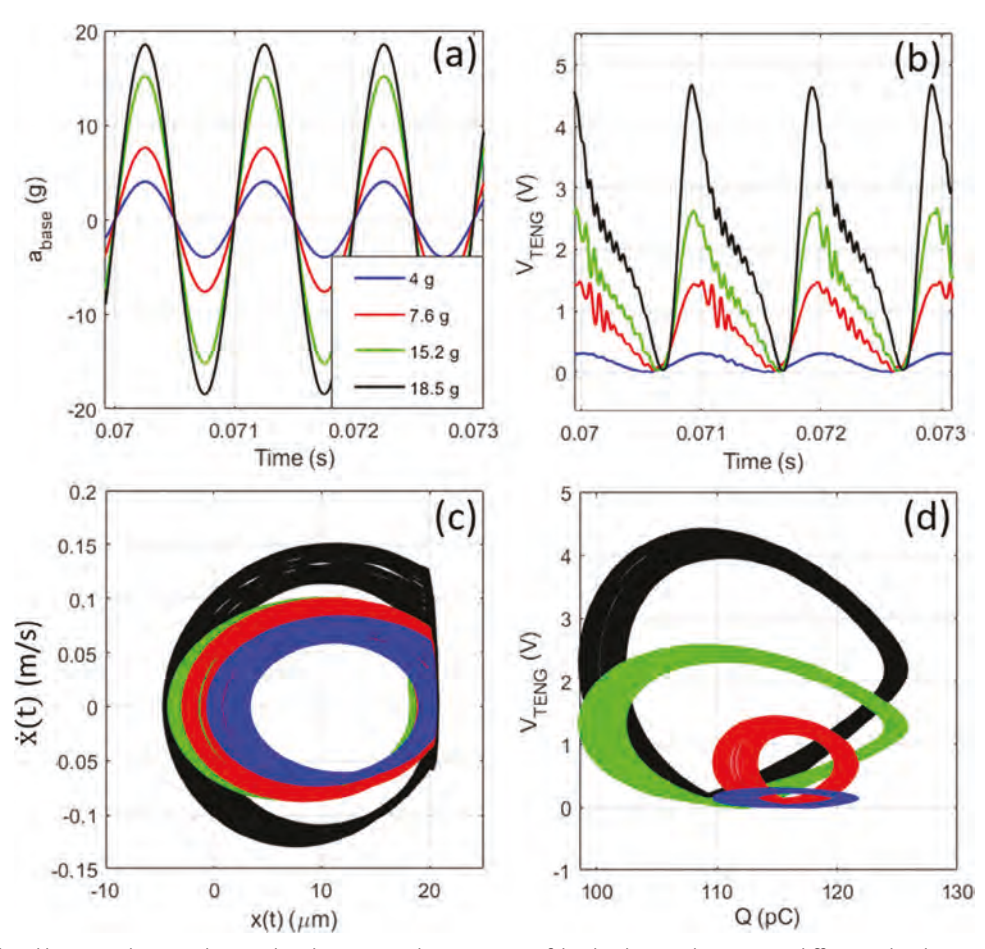


Figure 11. a) Simulated base acceleration. b) Simulated V_{TENG} . c) Phase-portrait of the diaphragm dynamics at different g-levels. x > 0 shows the position between the domed situation and the polyimide. $\dot{x} > 0$ shows the motion toward the polyimide. d) Phase-portrait of the accumulated charge Q and the induced potential difference ($R\dot{Q}$). Black plots: 18.5g, green plots: 15.2g, red plots: 7.6g, blue plots: 4g.

results in the difference in the approximation of the mass for the lumped system.

The initial air gap $d_{\rm warp} \approx 20\,\mu{\rm m}$. The rest of the unknown parameters will be the charge density, σ_t , and the internal resistance of the device, R. We considered the warped MEMS-TENG output at 1 kHz and 4g in Figure 7a as the benchmark. **Figure 11**b shows the time response of the MEMS-TENG model to input base excitation shown in Figure 11a, where g-levels are 4g, 7.6g, 15.2g, and 18.5g at 1 kHz. The reason for this choice is that we

Table 2. Comparison between the conventional^[30] MEMS-TENG design with springs in contact-separation mode and the presented design with curled diaphragm and direct attachment of diaphragm on dielectric instead of serpentines.

| Criteria | 2 μm gap (original ^[28]) | 20 μm gap (this work) |
|-----------------|--------------------------------------|-----------------------|
| Operation range | 2–10g | 0.5–67g |
| Bandwidth | 100–7000 Hz | 100-12 000 Hz |
| Output range | 0-0.7 V | 0-8 V |
| Sensitivity | 70mVg^{-1} | $300 \rm mVg^{-1}$ |
| SNR | 23 dB @ 1g, 1 kHz | 30 dB @ 1g, 1 kHz |

have measured $V_{\rm TENG}$ in identical base-excitations as reported in Figure 7a. Using the experimental result measured in the presence of 1 kHz and 4g external vibration, the unknown parameters R and σ_t are obtained to be 70 M Ω and 1.7 μ Cm², respectively. The obtained resistance is smaller than the value obtained in the original MEMS-TENG reported in refs. [28-30]. Noise is considered as an uncontrolled random input in Equation (7). As in Figure 9, the noise infinity norm is 0.0027 V. Figure 11a,b shows the simulated time-history at the benchmark and some larger g-levels (7.6g, 15.2g, and 18.5g). Similar to the experimental results, the shape of the generated signal at 4g and 7.6g follows the base-excitation. Although $V_{\rm TENG}$ follows the tone of the external vibration, a sharp decay in the signal shape is observed for a portion of time. The signal shape and magnitudes of V_{TENG} match the experiments in the linear range. However, the simulation results underestimate the generated voltage. The difference originates from the assumption of constant charge density. The phase portrait of the diaphragm motion in Figure 11c shows with increasing the g-level, the diaphragm oscillation amplitude is increased. In all conditions, the motion is blocked by the polyimide layer during contact-separation in $x \approx d_{\text{warp}}$. The velocity range is wider at higher g-levels. For a better understanding on the relation between the accumulated charge and generated voltage,

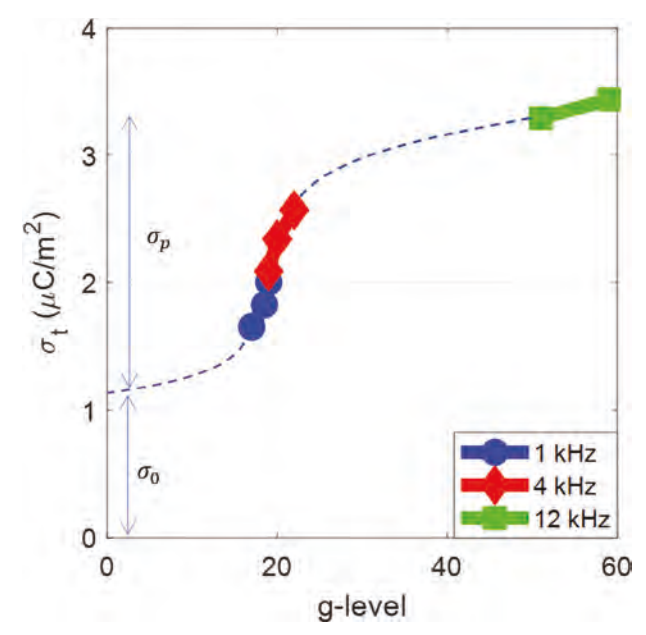


Figure 12. Calculated charge density using the measurements during the operation in nonlinear mode.

another phase portrait is plotted in Figure 11d. The linearity of the operation at low g-levels is shown in the red and blue graphs as they look like elliptical, compared to the nonlinear range which appears in almond shape as in green and black graphs.

A more precise model should account for the larger charge density over the polyimide because of the stronger impacts at the boundaries and center of the diaphragm. Considering the output of the MEMS-TENG at a constant frequency, for example, f =1 kHz, the larger g-levels cause larger output in both modes (see Figure 7a). Our goal is to investigate the reasons for the dependence of the sensor output on the g-level of the external vibration. The effect of the g-level on the charge density is denoted by $\sigma_{\rm p}(a_{\rm base})$ in Equation (8). Considering the linear mode at g-levels less than 15.2g, the difference in the amplitude of the MEMS-TENG output at different g-levels originate from the different displacements and larger charge densities at larger g-levels. To study the effect of g-level on the charge density, the results in nonlinear mode are considered where the diaphragm displacement is not a changing ($x \approx 0$). At different g-levels, the experimental results are used in Equation (27) to calculate the total charge density. Figure 12 demonstrates the results for three frequencies of 1, 4, and 12 kHz. In the presence of a 1 kHz base excitation, increasing the g-level from 17g to 19g causes the charge density to change from 1.654 to 2.002 μCm^{-2} . In the presence of a 4 kHz base excitation, increasing the g-level from 19g to 22g causes the charge density to change from 2.089 to 2.571 μ C m^{-2} . In the presence of a 12 kHz base excitation, increasing the g-level from 51g to 66g causes the charge density to change from 3.292 to 3.440 μ Cm⁻². Increasing the g-level results in more inertial force between triboelectric layers during the oscillation. Because of the limitations in the experimental setup, the g-level intervals that do not have experimental results are shown with dashed lines. By estimating the charge densities at g-levels we could not produce on the shaker, we can produce a range of densities for g-levels from zero

through 60. The densities rise rapidly around 20g but then slow down as they near 60g. The g-level boosts the charge density because of the larger impact during the contact separation in the diaphragm center and attached boundaries.

To investigate V_{TENG} during the linear and nonlinear modes, we plug the maximum air gap into Equation (7) to calculate where the nonlinearity first appears as shown in Figure 2d. This equation is a nonlinear first order differential equation that has two parts, a decaying part that is the coefficient of the charge, and an input part that is the main factor represented by the $V_{\rm TENG}$. A triboelectric motion sensor is basically expected to detect and convert the base-excitation a_{base} into an electrical output. The transduction starts from first absorption of the kinetic energy of the external vibration a_{base} and its conversion into the diaphragm motion. Second, the mechanical to electrical transduction converts the diaphragm displacement d(t) into the electrical potential difference $V_{TENG} = R\dot{Q}$. We will focus on the electrical transduction in this work. In the presence of vibrational motions, an ideal tracking performance should provide the least phase shift and a significant amplification that is the maximization of the inputto-output gain. Considering the dynamics of the diaphragm in Equation (1), the effect of the base-excitation force Equation (3) is two orders of magnitudes larger than the electrostatic force. For simplification, we neglect Equation (6) in the following analysis and consider d(t) as an independent input to Equation (7). This equation contains the effect of the external vibration in the decaying part which is nonlinear because of the multiplication of the motion (d) into the system state (Q), and second in the linear input term. Assuming a harmonic diaphragm motion as $d(t) = D\sin(2\pi ft)$ where D is the diaphragm oscillation amplitude. Equation (7) will become:

$$\dot{Q} = -\frac{t_{\rm p}/\epsilon_{\rm r} + D\sin(2\pi f t)}{R\epsilon_0 A}Q + \frac{\sigma_t}{R\epsilon_0}D\sin(2\pi f t)$$
 (18)

The nonlinearity in electrical transduction becomes significant when the D is in the same order or larger than the polyimide thickness $t_{\rm p}/\epsilon_{\rm r}$. In the mesoscale, the order of magnitude of the diaphragm motion is large and comparable with the dielectric thickness which explains why a sharp nonlinear signal is observed. However, in MEMS scale, the diaphragm can travel minute displacements that are remarkably smaller than the polyimide thickness, and therefore, a linear operation range is achievable in the MEMS scale. In this condition, we can assume that $D \ll t_{\rm p}/\epsilon_{\rm r}$ and therefore, the differential equation becomes:

$$\dot{Q} = -\frac{t_{\rm p}}{R\epsilon_0 \epsilon_{\rm r} A} Q + \frac{\sigma_{\rm t}}{R\epsilon_0} D \sin(2\pi f t)$$
 (19)

By solving Equation (19) the accumulated charge as a result of the diaphragm vibrations is obtained as:

$$Q(t) = Q_0 \sin(2\pi f t - \phi) \tag{20}$$

where Q_0 and ϕ are the induced charge amplitude and the phase delay and are defined as:

$$Q_0 = \frac{\sigma_t D A \epsilon_r}{\sqrt{t_p^2 + (R \epsilon_0 \epsilon_r A 2 \pi f)^2}}$$
 (21)

(6136829, 0, Downloaded from https://onlinelibrary.wiley.com/doi/10.1002/smll.202304591 by Test, Wiley Online Library on [02/11/2023]. See the Terms and Conditions (https://onlinelibrary.wiley.com/terms-and-conditions) on Wiley Online Library for rules of use; OA articles are governed by the applicable Creative Commons. Licenses

$$\phi = \tan^{-1}(2\pi f R \epsilon_0 \epsilon_r A/t_p) \tag{22}$$

The generated potential difference is then calculated by multiplying the derivative of *Q* in Equation (20) by the internal resistance

$$V_{\text{TENG}} = \frac{2\pi f \sigma_{\text{t}} D}{\epsilon_0 \sqrt{\left(\frac{t_{\text{p}}}{R_{\text{e.e.}A}}\right)^2 + (2\pi f)^2}} \cos(2\pi f t - \phi)$$
 (23)

Equation (23) reveals a linear relationship between the diaphragm oscillation amplitude and the output voltage. The polyimide thickness decreases the V_{TENG} , while the diaphragm area A boosts it. An important factor that limits the miniaturization of TENG is the diaphragm area reduction because of the significant decrease in the potential difference. However, Equation (23) reveals that reducing the polyimide thickness increases the charge density and the diaphragm range of motion which can increase the generated voltage, which is an advantages for enhancing the SNR of event-driven devices.

The voltage output of the TENG is linearly proportional to the amplitude of the displacement (D) when the displacement has a harmonic profile as indicated in Equation (23). The displacement maintains a harmonic profile at low excitation levels. Higher voltage and greater SNR are obtained because of increase of range of motion of the TENG using the dome-shaped structure, which increased the initial height from 2 µm in our previous work [1] to 20 µm in the present study. Also, the engagement of the periphery of the dome-shaped structure with the underneath polyimide increases σ_t in Equation (23), which further increases the output voltage and the SNR. Once the excitation level increases, the displacement will include higher order harmonics and the relationship between maximum output voltage and the amplitude will be nonlinear. However, the increase of the initial gap and charge density by employing the dome-shaped structure would still increase the output voltage.

Because of the particular dynamics of the TENG in the contactseparation mode and the hardening stiffness of the diaphragm in its arch-shaped structure, the diaphragm remains steady during the time interval that the diaphragm is dome-shaped in the presence of a large base excitation. At this moment, Equation (7) is rewritten with $d \approx d_{\text{warp}}$ as:

$$\frac{V_{\text{TENG}}}{R} = \dot{Q}(t) = -\frac{t_{\text{p}}/\epsilon_{\text{r}} + d_{\text{warp}}}{\epsilon_{\text{o}} A R} Q(t) + \frac{\sigma_{\text{t}} d_{\text{warp}}}{\epsilon_{\text{o}}}$$
(24)

Equation (24) indicates the charge transfer during the warped position. This equation is a decaying first-order differential equation and is written as:

$$\dot{Q}(t) = -\frac{1}{RC}Q(t) + \frac{\sigma_t d_{\text{warp}}}{R\epsilon_0}$$
 (25)

where $C = \frac{\epsilon_0 A}{t_p/\epsilon_r + d_{\text{warp}}}$ is the decaying coefficient and $\frac{\sigma_t d_{\text{warp}}}{R\epsilon_0}$ is the charge density effect that is the forcing function in this equation. Time-response of the static charge Q(t) is calculated as:

$$Q(t) = \frac{\sigma_t A d_{\text{warp}}}{t_p / \epsilon_r + d_{\text{warp}}} (1 - e^{-\frac{t}{RC}})$$
 (26)

The voltage response is obtained by derivative calculation of Equation (26) as:

$$V_{\text{TENG}}(t) = \frac{\sigma_{\text{t}} d_{\text{warp}}}{\epsilon_{0}} e^{-\frac{t}{RC}}$$
(27)

Equation (27) shows that at the arch-shaped position where the system has the highest stiffness, V_{TENG} keeps decaying exponentially until returning to the linear mode. Moreover, it describes that the diaphragm curl, air gap and charge density linearly increase the generated voltage. Because the generated voltage for the nonlinear modes overlap on the same decaying function, we can conclude that the air gap is nearly steady when the diaphragm is in the curled-up position (see Figure 7e,f). However, larger outputs are observed by increasing the g-level. Although d_{warp} is nearly constant at different g-levels, the question is what causes this difference. Considering Equation (27) the difference is due to the larger charge density in the presence of larger vibrations because of the direct contact and permanent friction between the pair of triboelectric layers.

As in Equation (27), the maximum output that the MEMS-TENG output can reach is $\bar{V}_{\text{TENG}} = \sigma_{\text{t}} d_{\text{warp}} / \epsilon_0$. The latter equation analytically proves that for maximizing the sensor output, the diaphragm warp height (d_{warp}) and charge density (σ_t) should be maximized. Increasing the warp height depends on the MEMS fabrication techniques that enable larger heights as in Figure 2f.

4. Conclusion

Triboelectric vibration sensors in contact-separation mode are well-known for their remarkable voltage and minute power generation as well as event-driven operation. However, miniaturizing them into microscale devices adversely affects the output voltage magnitude and signal-to-noise ratio. We presented two design ideas to boost the output and operation range. The latest MEMS triboelectric vibration sensor contains the typical components including a conductive flat diaphragm hinged above a dielectric layer using springs. This work presents a MEMS design without springs where the diaphragm is a dome-shaped micro plate and is attached to the dielectric at the boundary. In contrast to the conventional design, which only operates when the g-level is larger than the contact threshold, the current device produces charge density continuously because of the permanent contact between the metal and dielectric at the adhered boundaries. Experimental results show that the amount of charge density production depends on the vibration g-level, which determines how much friction occurs between triboelectric layers. Second, using a dome-shaped diaphragm profile, a larger range of motion is provided after contact-separation which results in one order of magnitude larger output voltage as reported in the analytical and experimental results. In addition, the device operates at one order of magnitude larger g-levels as a result of the large gap between electrodes. Results show improvements in SNR, sensitivity, and robustness. The presented electromechanical model reveals that triboelectric motion sensing operates in two regions: linear, for low amplitude vibrations, and nonlinear, for stronger vibrations where the diaphragm displacement is relatively large.

5. Experimental Section

MEMS-TENG Fabrication Process: The fabrication process of the MEMS triboelectric generator used in this paper was reported in ref. [28]. In summary, the process started with an aluminum nitride layer to insulate the conductive wafer, then, the first conductive layer of the triboelectric generator was a sputtered chrome-aluminum layer patterned with inductive-conductive plasma (ICP). Then, a thick film of polyimide was spun and cured in an oven to create the polyimide-aluminum triboelectric pair. The polyimide was followed with a silicon oxide sacrificial layer which was patterned with reactive ion etching (RIE). Then, another aluminum film was sputtered for the top electrode followed by a physical vapor deposition of amorphous silicon that was used as a proof mass and as a stress neutralizer since it converted the stresses of the aluminum layer from compressive to a tensile for the aluminum-amorphous silicon pair. This pair was patterned by RIE and ICP, respectively. Then, wafer was diced and dies were released and wire-bonded to create the device.

Electrostatic Actuation of MEMS TENG Diaphragm: For electrostatic actuation, the top and bottom electrodes were connected to the input voltage that was generated in the computer, sent to the DAQ, and transferred to the voltage amplifier.

MEMS-TENG Output Analysis: The electrical output of such sensors was an induced potential difference that is an indicator of the external motion. An electrodynamic shaker B&K 4809 was used for generating the external vibrations. The potential difference V_{TENG} between the two movable and fixed electrodes (see Figure 2d) was measured using a National Instruments 6366 USB data-acquisition system. This device contained 8 inputs that can sense and tolerate $\pm 10 \,\text{V}$. The input impedance between the terminals was reported as 100 pF in the data sheet. The mechanical characterization of a motion sensor was the analysis of the diaphragm motion. A laser Doppler velocimetry (LDV) was used for MEMS motion analysis. Electrodynamic shakers convert electrical energy to mechanical motion which was used to simulate the vibration of moving objects.

Acknowledgements

The authors would like to acknowledge the financial support of this study by the National Science Foundation (NSF) through Grant 1919608. This work was performed in part at the Cornell NanoScale Science & Technology Facility, a member of the National Nanotechnology Coordinated Infrastructure, which is supported by the National Science Foundation (Grant NNCI-2025233).

Conflict of Interest

The authors declare no conflict of interest.

Data Availability Statement

The data that support the findings of this study are available from the corresponding author upon reasonable request.

Keywords

accelerometer, inertial measurement, MEMS, motion sensors, triboelectric generators

> Received: May 31, 2023 Revised: October 6, 2023 Published online:

[1] V. Vyplaven, A. Kolomeets, A. Popkov, in International Scientific Siberian Transport Forum TransSiberia-2021, vol. 2, Springer, Cham 2022, pp. 313-323.

- [2] Q. Yang, T. Liu, X. Wu, Y. Deng, IEEE Access 2020, 8, 107161.
- [3] J. Chelvarajah, R. Lakshmanan, S. K. Selvaperumal, in J. Phys.: Conf. Ser. 2019, 1228, 012065.
- [4] D. T. Martin, J. Liu, K. Kadirvel, R. M. Fox, M. Sheplak, T. Nishida, J. Microelectromech. Syst. 2007, 16, 1289.
- [5] M. Daeichin, R. N. Miles, S. Towfighian, IEEE Sens. J. 2020, 21, 3097.
- [6] S. T. Hansen, A. S. Ergun, W. Liou, B. A. Auld, B. T. Khuri-Yakub, J. Acoust. Soc. Am. 2004, 116, 828.
- [7] M. L. Kuntzman, N. A. Hall, J. Acoust. Soc. Am. 2014, 135, 3416.
- [8] J. Qin, L.-J. Yin, Y.-N. Hao, S.-L. Zhong, D.-L. Zhang, K. Bi, Y.-X. Zhang, Y. Zhao, Z.-M. Dang, Adv. Mater. 2021, 33, 2008267.
- [9] L. Chen, M. Lu, H. Yang, J. R. Salas Avila, B. Shi, L. Ren, G. Wei, X. Liu, W. Yin, ACS Nano 2020, 14, 8191.
- [10] M. Korrapati, S. Chauhan, Y. Tang, D. Gupta, Macromol. Mater. Eng. **2022**, *307*, 2200132.
- [11] R. Suzuki, T.-V. Nguyen, T. Takahata, I. Shimoyama, in 2019 IEEE 32nd International Conference on Micro Electro Mechanical Systems (MEMS), IEEE, Piscataway, NJ 2019, pp. 688-691.
- X. Han, Q. Mao, L. Zhao, X. Li, L. Wang, P. Yang, D. Lu, Y. Wang, X. Yan, S. Wang, N. Zhu, Z. Jiang, Microsyst. Nanoeng. 2020, 6,
- [13] M. L. Kuntzman, D. Kim, N. A. Hall, J. Microelectromech. Syst. 2014, 24, 404.
- [14] M. D. Williams, B. A. Griffin, T. N. Reagan, J. R. Underbrink, M. Sheplak, J. Microelectromech. Syst. 2012, 21, 270.
- [15] Q. Liu, X.-X. Wang, W.-Z. Song, H.-J. Qiu, J. Zhang, Z. Fan, M. Yu, Y.-Z. Long, ACS Appl. Mater. Interfaces 2020, 12, 8288.
- [16] B. H. Moghadam, M. Hasanzadeh, A. Simchi, ACS Appl. Nano Mater. 2020, 3, 8742.
- [17] J. Zhang, G. Chen, K. Zhang, D. Zhao, Z. Li, J. Zhong, ACS Appl. Mater. Interfaces 2022, 15, 2449.
- [18] L. Wang, M. Hu, K. Kong, J. Tao, K. Ji, Z. Dai, Nano Energy 2022, 104, 107934
- [19] S. Gong, J. Zhang, C. Wang, K. Ren, Z. L. Wang, Adv. Funct. Mater. **2019**, 29, 1807618.
- [20] D. W. Kim, J. H. Lee, J. K. Kim, U. Jeong, NPG Asia Mater. 2020, 12, 6.
- [21] X. Qu, J. Xue, Y. Liu, W. Rao, Z. Liu, Z. Li, Nano Energy 2022, 98,
- [22] M. Zhu, Z. Sun, T. Chen, C. Lee, Nat. Commun. 2021, 12, 2692.
- [23] Y. Lu, H. Tian, J. Cheng, F. Zhu, B. Liu, S. Wei, L. Ji, Z. L. Wang, Nat. Commun. 2022, 13, 1401.
- [24] N. A. Hossain, G. G. Yamomo, R. Willing, S. Towfighian, IIEEE/ASME Trans. Mechatron. 2021, 26, 2967.
- [25] A. Ibrahim, M. Jain, E. Salman, R. Willing, S. Towfighian, Smart Mater. Struct. 2019, 28, 025040.
- [26] H. Lei, Y. Chen, Z. Gao, Z. Wen, X. Sun, J. Mater. Chem. A 2021, 9,
- [27] H. A. Hamid, Z. Celik-Butler, in 2019 IEEE Sensors Applications Symposium (SAS), IEEE, Piscataway, NJ 2019, pp. 1-6.
- [28] M. Alzgool, M. Mousavi, B. Davaji, S. Towfighian, Nano Energy 2022, 103, 107758.
- [29] M. Mousavi, M. Alzgool, B. Davaji, S. Towfighian, MMech. Syst. Signal Process. 2023, 187, 109921.
- [30] M. Alzgool, Y. Tian, B. Davaji, S. Towfighian, Nano Energy 2023, 109,
- [31] L. Medina, R. Gilat, S. Krylov, Sens. Actuators, A 2016, 248, 193.
- [32] A. Frangi, G. Gobat, IInt. J. Non-Linear Mech. 2019, 116, 211.
- [33] A. Narimani, M. Golnaraghi, G. N. Jazar, JJ. Vib. Control 2004, 10,
- [34] M. Mousavi, M. Alzgool, S. Towfighian, Smart Mater. Struct. 2021, 30,
- [35] S. Niu, S. Wang, L. Lin, Y. Liu, Y. S. Zhou, Y. Hu, Z. L. Wang, Energy Environ. Sci. 2013, 6, 3576.
- C. Zhang, L. Zhou, P. Cheng, X. Yin, D. Liu, X. Li, H. Guo, Z. L. Wang, J. Wang, Appl. Mater. Today 2020, 18, 100496.

_ smal

16136289, 0, Downloaded from https://onlinelibrary.viely.com/doi/10.1002/smll.202304591 by Test, Wiley Online Library on [02/11/2023]. See the Terms and Conditions (https://onlinelibrary.wiely.com/terms-and-conditions) on Wiley Online Library for rules of use; OA articles are governed by the applicable Creative Commons License

www.advancedsciencenews.com

www.small-journal.com

- [37] M. Mousavi, M. Alzgool, S. Towfighian, IEEE Sens. J. 2021, 21, 18601.
- [38] J. Peng, S. D. Kang, G. J. Snyder, Sci. Adv. 2017, 3, eaap8576.
- [39] Y. Li, Z. Zhao, L. Liu, L. Zhou, D. Liu, S. Li, S. Chen, Y. Dai, J. Wang, Z. L. Wang, Adv. Energy Mater. 2021, 11, 2100050.
- [40] T. Du, F. Dong, Z. Xi, M. Zhu, Y. Zou, P. Sun, M. Xu, Small 2023, 2300401.
- [41] L. Liu, Z. Zhao, Y. Li, X. Li, D. Liu, S. Li, Y. Gao, L. Zhou, J. Wang, Z. L. Wang, Small 2022, 18, 2201402.
- [42] M. A. Adly, M. H. Arafa, H. A. Hegazi, Nano Energy 2021, 85, 105952.